JGR Atmospheres

RESEARCH ARTICLE
10.1029/2023JD038725

Probing Gravity Waves in the Middle Atmosphere Using Infrasound From Explosions

Ekaterina Vorobeva[1,2], Jelle Assink[3], Patrick Joseph Espy[1], Toralf Renkwitz[4], Igor Chunchuzov[5], and Sven Peter Näsholm[2,6]

[1]Department of Physics, Norwegian University of Science and Technology, Trondheim, Norway, [2]NORSAR, Kjeller, Norway, [3]R&D Seismology and Acoustics, Royal Netherlands Meteorological Institute (KNMI), De Bilt, The Netherlands, [4]Leibniz Institute of Atmospheric Physics, University of Rostock, Kühlungsborn, Germany, [5]Obukhov Institute of Atmospheric Physics, Moscow, Russia, [6]Department of Informatics, University of Oslo, Oslo, Norway

Abstract This study uses low-frequency, inaudible acoustic waves (infrasound) to probe wind and temperature fluctuations associated with breaking gravity waves (GWs) in the middle atmosphere. Building on an approach introduced by Chunchuzov et al., infrasound recordings are used to retrieve effective sound-speed fluctuations in an inhomogeneous atmospheric layer that causes infrasound backscattering. The infrasound was generated by controlled blasts at Hukkakero, Finland, and recorded at the IS37 infrasound station, Norway in the late summers 2014–2017. Our findings indicate that the analyzed infrasound scattering occurs at mesospheric altitudes of 50–75 km, a region where GWs interact under non-linearity, forming thin layers of strong wind shear. The retrieved fluctuations were analyzed in terms of vertical wave number spectra, resulting in an approximate k_z^{-3} power law that corresponds to the "universal" saturated spectrum of atmospheric GWs. The k_z^{-3} power law wavenumber range corresponds to vertical atmospheric scales of 33–625 m. The fluctuation spectra were compared to theoretical GW saturation theories as well as to independent wind measurements by the Saura medium-frequency radar near Andøya Space Center around 100 km west of IS37, yielding a good agreement in terms of vertical wavenumber spectrum amplitudes and slopes. This suggests that the radar and infrasound-based effective sound-speed profiles represent low- and high-wavenumber regimes of the same "universal" GW spectrum. The results illustrate that infrasound allows for probing fine-scale dynamics not well captured by other techniques, suggesting that infrasound can provide a complementary technique to probe atmospheric GWs.

Plain Language Summary This study analyzes inaudible acoustic waves (infrasound) detected in Norway following explosions during disposal of military equipment in Finland. We show that infrasound reflects off small-scale structures in the middle atmosphere (within 50–75 km altitude) and we use signals recorded to retrieve so-called effective sound-speed profiles, a proxy of small-scale variations in temperature and horizontal wind. Spectral analysis of the retrieved altitude profiles reveals a power law associated with gravity waves (GWs). Such waves are important in the transfer of energy between atmospheric layers and are generated, for example, by upward air flow over mountain ranges. The vertical scales to which infrasound is sensitive to, are estimated to range from 33 to 625 m. Comparisons between spectra obtained using radar and infrasound show good agreement in terms of amplitudes and slopes. This suggests that the radar and infrasound-based effective sound-speed profiles represent different regimes of the same "universal" GW spectrum. This study uses a large, consistent infrasound data set and independent radar data to show that remote sensing of fine-scale wind and temperature variations in a region of the middle atmosphere for which very few observations are available, is possible by means of ground-based infrasound measurements.

Key Points:

- Ground-based infrasound recordings of explosions are used to retrieve effective sound speed fluctuations in the mesosphere
- Vertical wave number spectra of the retrieved fluctuations agree with the "universal" gravity wave saturation spectrum
- Infrasound from 49 explosions and radar data show that remote sensing of the middle atmosphere is possible via ground-based infrasound data

Correspondence to:
E. Vorobeva,
ekaterina.vorobeva@ntnu.no

Citation:
Vorobeva, E., Assink, J., Espy, P. J., Renkwitz, T., Chunchuzov, I., & Näsholm, S. P. (2023). Probing gravity waves in the middle atmosphere using infrasound from explosions. *Journal of Geophysical Research: Atmospheres*, *128*, e2023JD038725. https://doi.org/10.1029/2023JD038725

Received 18 FEB 2023
Accepted 16 JUN 2023

Author Contributions:
Conceptualization: Ekaterina Vorobeva, Jelle Assink, Sven Peter Näsholm
Formal analysis: Ekaterina Vorobeva
Funding acquisition: Patrick Joseph Espy, Sven Peter Näsholm
Methodology: Ekaterina Vorobeva, Jelle Assink, Patrick Joseph Espy, Igor Chunchuzov, Sven Peter Näsholm
Supervision: Jelle Assink, Patrick Joseph Espy, Sven Peter Näsholm
Validation: Ekaterina Vorobeva, Toralf Renkwitz
Visualization: Ekaterina Vorobeva, Jelle Assink
Writing – original draft: Ekaterina Vorobeva, Jelle Assink

1. Introduction

This study investigates the use of acoustic waves to probe fine-scale wind and temperature structures of the middle atmosphere (i.e., stratosphere and lower mesosphere). Atmospheric infrasound, that is, low-frequency sound waves in the inaudible frequency range (<20 Hz) can be generated by both natural (e.g., volcanoes, earthquakes, thunder) and artificial (e.g., rocket launches, sonic booms, blasts) sources. Once generated, infrasound waves can propagate in the atmosphere over long distances as the energy is ducted by waveguides formed by vertical gradients in temperature and wind (Brekhovskikh, 1960; Diamond, 1963). In addition to the source characteristics, infrasound waves also provide information about the medium through which they propagate, and

Writing – review & editing: Ekaterina Vorobeva, Jelle Assink, Patrick Joseph Espy, Toralf Renkwitz, Igor Chunchuzov, Sven Peter Näsholm

can therefore serve as a tool for atmospheric remote sensing (e.g., Assink et al., 2019; Chunchuzov et al., 2022; Le Pichon et al., 2005; Smets & Evers, 2014).

Probing the middle atmosphere by means of ground- and space-based remote sensing techniques contributes to a better representation of this region in atmospheric models. The latter allows for improved weather forecasts due to the dynamical coupling between different atmospheric layers (Shaw & Shepherd, 2008). The resolution of atmospheric models, and therefore the scales of atmospheric processes resolved, strongly depends on available computational capabilities and scientific applications. For example, high-resolution limited-area models routinely in use at national meteorological services (e.g., Bengtsson et al., 2017) have high horizontal resolution of several kilometers, however, the model top is typically in the lower stratosphere (∼10 hPa, or 30 km). In contrast, global numerical weather prediction models (NWPs) and general circulation models (GCMs) with model tops raised into the mesosphere and above (Stocker et al., 2014) have lower resolution and are unable to resolve atmospheric processes at scales smaller than 10 km in operational NWP (Bauer et al., 2015) and tens of kilometers in GCMs (Becker et al., 2022; H.-L. Liu et al., 2014).

While not fully resolvable by models, these subgrid-scale processes can be observed by various observational techniques, including radar, lidar and rocket measurements (Le Pichon et al., 2015; Rapp & Lübken, 2004; Schäfer et al., 2020; Strelnikov et al., 2019). One such subgrid-scale phenomenon is atmospheric gravity waves (GWs). Generated in the lower atmosphere, GWs propagate into the middle atmosphere with increasing amplitude due to the decrease in air density with altitude, until they ultimately become unstable and break. When breaking, GWs generate small-scale eddies or turbulence which in turn interact with other atmospheric waves (Fritts & Alexander, 2003). The transfer of energy and momentum between different atmospheric layers is an important function of atmospheric waves. For example, the middle atmospheric meridional circulation is primarily GW-driven (Fritts & Alexander, 2003) and breaking mesospheric GWs play an important role in the wintertime polar stratospheric downward motion (Garcia & Boville, 1994; Wicker et al., 2023). Momentum deposited by GWs (or GW drag) can modify atmospheric circulation patterns at lower altitudes, therefore affecting the weather and its prediction (McFarlane, 1987). This highlights the need for GW probing and for improvement of GW representation in NWP and GCMs. Efforts are also being made to develop GW-resolving GCMs stretching up to the edge of the thermosphere (e.g., Becker et al., 2022; H.-L. Liu et al., 2014).

GWs interact with other atmospheric waves in various ways, including wave-wave interaction and wave-breaking (Fritts & Alexander, 2003), and cause the presence of localized, three-dimensional small-scale fluctuations in temperature and wind fields. These have been observed in the middle atmosphere by in-situ, ground- and space-based instruments (e.g., Bossert et al., 2015; Fritts & Alexander, 2003; Miller et al., 2015; Podglajen et al., 2022; Selvaraj et al., 2014; Tsuda, 2014). The vertical scales of these fluctuations are significantly smaller than the horizontal scales, and have characteristic vertical length scales ranging from tens of meters to tens of kilometers (Gardner et al., 1993). The presence of such small-scale atmospheric fluctuations is known to affect propagation and scattering of infrasound waves (Chunchuzov & Kulichkov, 2020). Moreover, it has been demonstrated by Bertin et al. (2014) and Lalande and Waxler (2016) that infrasound waveguides are very sensitive to GW induced small-scale fluctuations in wind and temperature (see also Brissaud et al., 2023). This implies the importance of accounting for fine-scale atmospheric structures when modeling infrasound propagation (Chunchuzov et al., 2022; Drob et al., 2013; Hedlin & Drob, 2014). On the other hand, this also suggests that infrasound observations can be used to probe small-scale atmospheric fluctuations, thereby addressing the need for an enhanced observations of GWs (Cugnet et al., 2019).

The purpose of the current study is to quantify GW activity using a data set of infrasound recordings from distant ground-based explosions. These signals have been recorded at a ground-based microbarometer array in Norway, every day during the period of mid-August to mid-September for the years 2014–2017. We apply a method that allows for the retrieval of so-called effective sound speed fluctuations in an inhomogeneous layer in the middle atmosphere. The method was developed over several years by Chunchuzov (2002), Chunchuzov et al. (2013, 2015, 2022), and Chunchuzov and Kulichkov (2020). Based on the retrieved effective sound speed fluctuations for each event, we calculate the corresponding vertical wavenumber spectrum, and further interpret this in terms of power spectral density (PSD) slope and amplitude. The retrieved GW spectra are further compared to independent wind radar observations as well as to both linear and non-linear theoretical GW saturation models (Dewan & Good, 1986; Chunchuzov et al., 2015; S. A. Smith et al., 1987).

We exploit an infrasound data set of signals generated by ground-based blasts in Hukkakero, Finland. These signals are detected at 321 km distance from the source, at microbarometer array IS37 in Northern Norway. This data set has several attractive features making it suitable for atmospheric probing studies. First, the explosive events take place during August and September which is during the atmospheric transition from summer to winter, when the zonal component of the stratospheric winds reverses from westward to eastward (Waugh & Polvani, 2010; Waugh et al., 2017). Second, the known locations of the source and receiver together with the transient nature of the blasts make it possible to clearly identify arrivals from both stratospheric and from mesospheric—lower thermospheric (MLT) altitudes. Finally, yet importantly, the recurring nature of explosive events allows us to study day-to-day variability of the middle atmosphere dynamics.

The paper is organized as follows. A background on infrasound sensitivity to atmospheric structure, infrasound signal processing terminology, and previous studies exploiting Hukkakero explosion-related data is provided in Section 2. Section 3 describes the infrasound data set, signal pre-processing, the SD-WACCM-X atmospheric model used, and the ray-tracing simulations conducted. Its Section 3.4 elaborates the effective sound speed retrieval methodology. The obtained results are shown in Section 4, also further discussed in Section 5 including vertical wavenumber spectrum comparison to independent radar measurements and theoretical models.

2. Background

2.1. Sensitivity of Infrasound to Atmospheric Structure

Infrasound propagation is sensitive to spatial variations in temperature and wind (e.g., Waxler & Assink, 2019). In the direction of propagation, the wind and temperature related propagation effects can approximately be modeled using the concept of effective sound speed, $C_{\text{eff}}(z)$, defined as:

$$C_{\text{eff}}(z) = \sqrt{\gamma RT} + \mathbf{u} \cdot \hat{n}, \tag{1}$$

where, γ, R, T, $\mathbf{u}$, and $\hat{n}$ correspond to the adiabatic index, the specific gas constant for air, the absolute temperature, the horizontal wind speed vector and the direction of propagation, respectively. Up to ∼100 km altitude, the Earth's atmosphere is well mixed, and it is appropriate to approximate $\sqrt{\gamma R} \approx 20\,\text{m}\,\text{s}^{-1}\text{K}^{-1/2}$. For cases where ground-to-ground propagation is of interest, it is convenient to introduce the effective sound speed ratio, which is obtained by normalizing $C_{\text{eff}}(z)$ by its value on the ground and which is analogous to the more familiar refractive index. From classical ray theory, acoustic signals that originate from the ground are expected to traverse in waveguides between the ground and the altitudes for which the C_{eff} ratio exceeds unity.

The celerity is defined as the source-receiver great-circle distance divided by the infrasound travel time (i.e., the difference between the arrival time and origin time). The celerity can hence be considered as the average group speed of a guided acoustic wave. When the origin time and location are known, celerity-based models can be used to provide information about the infrasound waveguide through which an acoustic wave propagated. Infrasonic paths with a substantial vertical component have a group speed that is significantly lower than the speed of sound. Conversely, infrasound guided by tropospheric waveguides (that propagates in the troposphere) has a celerity near the local sound speed. Typical celerities for different waveguides are 310–330 m/s for tropospheric arrivals, 280–320 m/s for stratospheric arrivals, and 180–310 m/s for mesospheric and thermospheric arrivals (e.g., Lonzaga, 2015; Nippress et al., 2014).

2.2. Infrasound Array Processing

An infrasound array is a group of microbarometers distributed in space but installed close enough so that the received sensor signals are sufficiently coherent to estimate the wavefront parameters of the dominant plane wave arriving at the array. This is done using array signal processing techniques that delay and sum sensor traces according to a model for the inter-element delays. This spatial filtering allows for reducing incoherent noise and for separating acoustic signals from different directions of arrival. Identification of the signals of interest is typically based on the observed back-azimuth, apparent velocity, and average inter-sensor coherence. The back-azimuth represents the direction from which the plane wave arrives at the array and is measured in degrees clockwise from the North. The apparent velocity is the velocity the plane wave appears to travel at horizontally along the array. This parameter is estimated based on the time delays between the sensors (as well

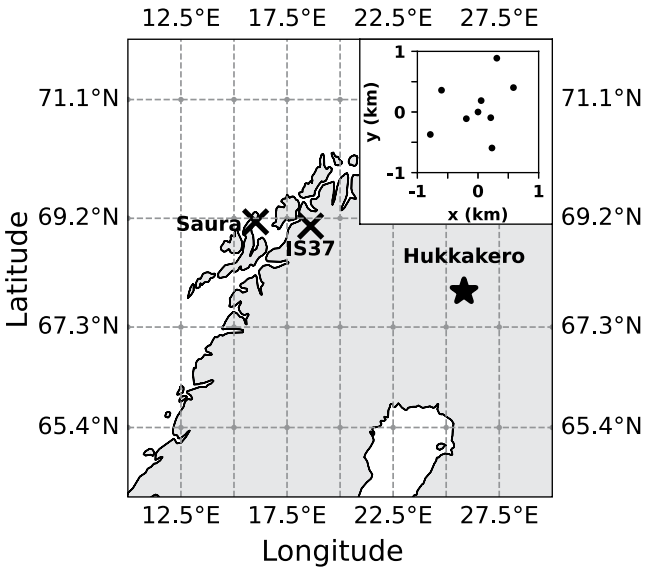

Figure 1. Location of all sources of data used in this study: Hukkakero explosion site, IS37 infrasound array, and Saura medium-frequency radar. The SD-WACCM-X atmospheric model grid is displayed on the map as gray dashed lines. The IS37 array layout is shown in the inset.

as back-azimuth) and contains information about the angle of incidence θ of the plane-wave, $v_{app} = c/\sin\theta$ where c is the local sound speed. There is no unique relationship between apparent velocity and altitude from which signal arrives, however higher values of apparent velocity would normally indicate arrival from higher altitudes. The combination of back-azimuth and travel time allows for signal identification and infrasound source location, while v_{app} helps to identify the incidence angle of the ray-path at the ground.

2.3. The Hukkakero Blasts in Infrasound Studies

The site of Hukkakero, Finland (67.94°N, 25.84°E; Figure 1), has been of particular interest for infrasound related studies over the past years. At Hukkakero, blasts related to the disposal of military explosives occur yearly since 1988 in August-September, typically once a day with a yield of around 20 tons of TNT equivalent (Gibbons et al., 2015). In addition to generating an atmospheric pressure wave, these explosions produce clear seismic signals which allow for the accurate estimation of origin time and location by means of seismic localization techniques (Gibbons et al., 2020). Blixt et al. (2019) showed that the ARCES seismic array in northern Norway records, besides the seismic waves, the ground-coupled airwaves associated with Hukkakero explosions. These explosions are also well-represented in event bulletins like the comprehensive European Infrasound Bulletin (Pilger et al., 2018, Figure 10), as well as in the Comprehensive Nuclear-Test-Ban Treaty (CTBT) bulletin products.

Infrasound signals that originated from Hukkakero explosions have been exploited in several atmospheric probing studies. Blixt et al. (2019) analyzed 30 years of Hukkakero explosions detected at the ARCES/ARCI seismo-acoustic array (Norway) in terms of back-azimuth deviation due to cross-wind (the component of wind perpendicular to the direction of propagation) along the propagation path. The resulting cross-wind estimates obtained showed a good agreement with the European Centre for Medium-Range Weather Forecasts (ECMWF) Reanalysis (ERA)-Interim model. Amezcua et al. (2020) and Amezcua and Barton (2021) presented a way to implement an off-line assimilation of infrasound data into atmospheric models using Ensemble Kalman filters. The study extends the approach by Blixt et al. (2019), demonstrating that assimilation of back-azimuth deviation allows for corrections to atmospheric winds at tropospheric and stratospheric altitudes. Based on the same data set, Vera Rodriguez et al. (2020) developed an extended inversion methodology that uses infrasound observations to update atmospheric wind and temperature profiles on the basis of the ERA5 re-analysis ensembles.

Still, Hukkakero related infrasound signals have not previously been used to probe small-scale atmospheric inhomogeneities.

3. Materials and Methods

3.1. Infrasound Data Set and Signal Pre-Processing

This study exploits Hukkakero explosions and the associated signals recorded at infrasound array IS37, located at ~320 km distance in Bardufoss, Norway (69.07°N, 18.61°E; Figure 1). This 10-element array is part of the International Monitoring System (IMS) for the verification of the CTBT (Marty, 2019). The region is also host to a cluster of additional seismo-acoustic monitoring stations (Gibbons et al., 2015). During the years 2014–2017, 57 explosions took place at Hukkakero, however 8 of them (the last three explosions in 2014 and the last five explosions in 2016) were significantly weaker (Gibbons et al., 2015) and are therefore not considered in the current study. Origin times of the analyzed 49 explosions are tabulated in Appendix A.

For each explosion, the back-azimuth and apparent velocity of the dominant wavefront were estimated using a conventional time-domain array processing technique (Melton & Bailey, 1957). The detection of coherent infrasound over the array is based on the evaluation of the so-called Fisher ratio. The Fisher ratio corresponds to a probability of detection of a coherent signal with a specific signal-to-noise ratio (SNR). The associated

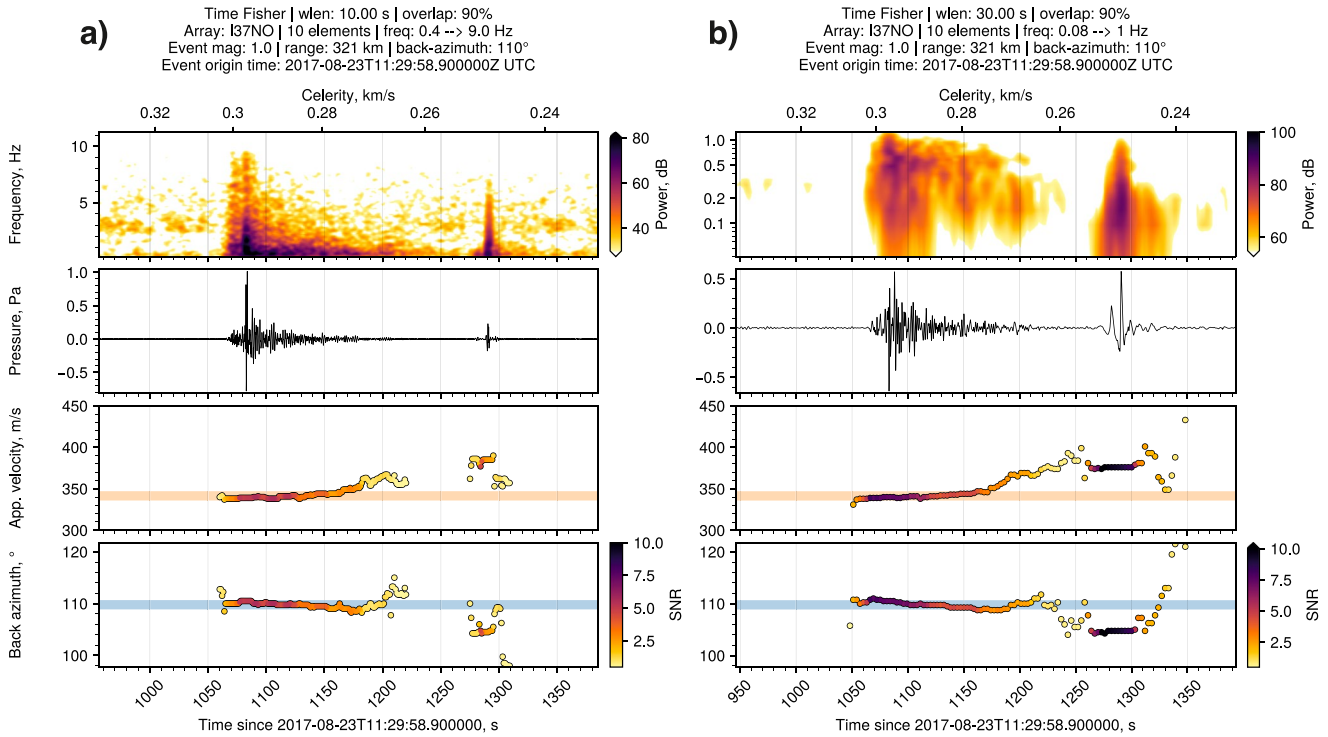

Figure 2. Array processing results for a Hukkakero explosion on 23 August 2017, processed between (a) 0.4–9 Hz and (b) 0.08–1.0 Hz. Top panel: spectrogram displayed in decibels. Second panel: the best-beam trace. Third panel: apparent velocity with an orange line indicating the sound speed on the ground (≈340 m/s). Bottom panel: the back-azimuth, where the blue line corresponds to the great-circle back-azimuth (110°) toward Hukkakero.

inter-element time-delays are used to form the so-called best-beam, for which the individual array recordings are time-aligned before summation. Details on the particular implementation can be found in Evers (2008). The beam waveforms were processed in two partly overlapping frequency bands to highlight the key trace features, 0.4–9 Hz and 0.08–1.0 Hz. Figure 2 shows array analysis results for one explosion filtered in both frequency bands. Note, the contribution of ocean ambient noise ("microbaroms") around 0.2 Hz (De Carlo et al., 2020; Vorobeva et al., 2021) and wind noise at low frequencies is negligible compared to the explosion contributions.

Figure 3 shows a compilation of IS37 infrasound signals from the 49 explosions exploited in the current study. The first arrivals are detected between 17.5 and 19 min (celerity of 281–314 m/s) after the explosion (Figure 3a) and feature energy in a broad frequency band (Figure 2a). Typically, the waveform consists of a main arrival with a significantly larger amplitude, followed by a coda ("tail") with progressively increasing apparent velocity with values within 340–360 m/s. These ranges of celerities and apparent velocities are typical for stratospheric arrivals (Lonzaga, 2015; Nippress et al., 2014) which generally refract or reflect near the stratopause. Similarly extended wave trains have been observed in far-field infrasound recordings following large detonations (Fee et al., 2013; Green et al., 2018; Lalande & Waxler, 2016), and it was assumed that these wave trains originate from interactions with atmospheric perturbations caused by GWs.

After this first wave train, a later arrival can in many cases be observed between approximately 20–23 min after the explosion (a celerity range of 232–267 m/s). Figures 2 and 3b show the signals in a pass-band between 0.08 and 1.0 Hz. This arrival is characterized by a clean, long period waveform (often of U shape), has higher apparent velocity values (i.e., >360 m/s) and larger back-azimuth deviations compared to the first arrival. All of these characteristics are typical of arrivals returning from the lower thermosphere (Assink et al., 2012, 2013; Blom & Waxler, 2021; Green et al., 2018; Le Pichon et al., 2005).

A closer look at Figure 3 further reveals that several of the events feature an arrival between the stratospheric and thermospheric arrivals, see also Gibbons et al. (2019, Figure 10.7). Although the current study only exploits the stratospheric arrivals for atmospheric probing, it is worth noting the potential for further analysis and probing based on later arrivals in the wavetrains, for example, as demonstrated in Chunchuzov et al. (2011).

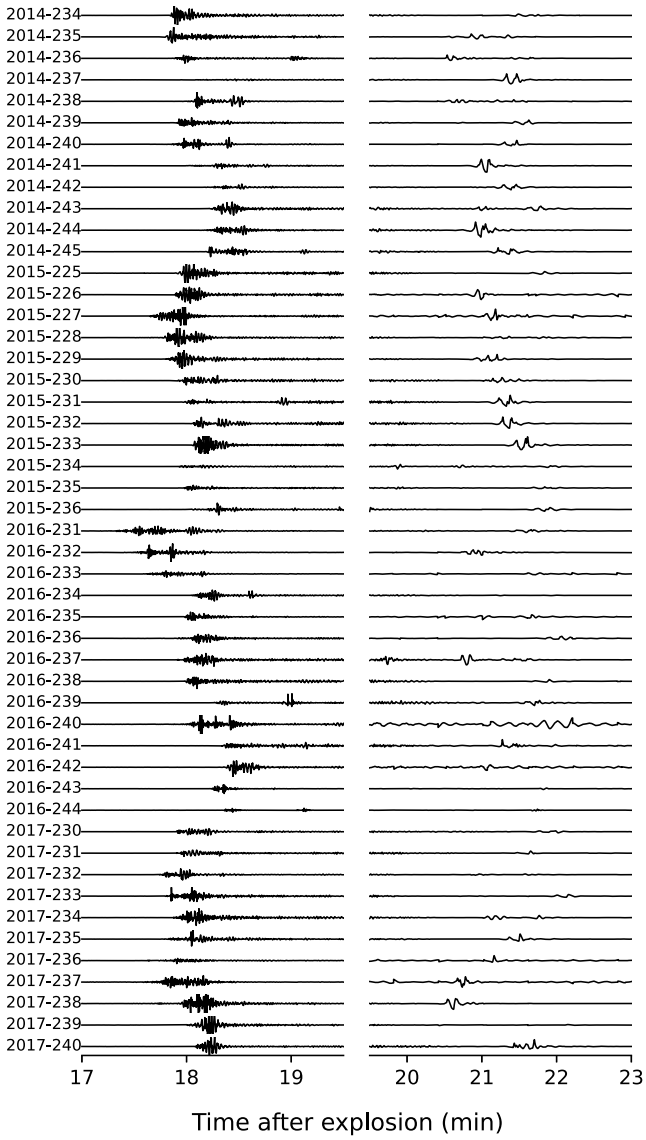

Figure 3. Infrasonic signals from 49 Hukkakero explosions that occurred in the time period 2014–2017. The signals have been recorded at infrasound array IS37 between (left) 17–19.5 min and (right) 19.5–23 min. The data are band-pass filtered between (left) 0.4–9 Hz and (right) 0.08–1 Hz. The *y*-axis of each trace has ±1 Pa limit. The left-hand side labels display the year and the day-of-year when events took place.

3.2. Atmospheric Data Sets

3.2.1. The Saura Medium-Frequency (MF) Radar

Another source of data used in this study is the Saura medium-frequency (MF) radar near Andøya, Norway (69.14°N, 16.02°E; Figure 1). Wind measurements provided by this radar are exploited in Section 4 to validate the results obtained using infrasound observations described in Section 3.1. The radar is located ∼100 km west of the IS37 infrasound station and ∼420 km north-west of Hukkakero, and operates on 3.17 MHz with fifty-eight 2 kW pulsed transceiver modules. Its observation capabilities include wind measurements, estimates of turbulent kinetic energy dissipation rates, and electron density, as well as meteor observations. The observations typically provide measurements within the ∼50–100 km altitude range with a vertical resolution of 1–1.5 km (Singer et al., 2008). The wind data used for the validation has been derived from Doppler-Beam-Swinging experiments measuring the radial velocity for one vertical and four oblique soundings including statistical interferometric Angle of Arrival correction (see Renkwitz et al., 2018).

3.2.2. The SD-WACCM-X Atmospheric Model

In this study, the Whole Atmosphere Community Climate Model with thermosphere and ionosphere extension (WACCM-X; H.-L. Liu et al., 2018) is used as a model atmosphere to simulate infrasound propagation. The WACCM-X is an extension of the WACCM (top at around 130–140 km) that includes additional physics and chemistry processes to simulate the ionosphere and thermosphere. The particular version of WACCM-X used in this study is the *specified dynamics*, SD-WACCM-X, version v2.1 (Sassi et al., 2013), for which the temperature and winds are nudged by the Modern-Era Retrospective analysis for Research and Applications, Version 2 (MERRA-2; Gelaro et al., 2017) from the ground up to ∼50 km. Above that altitude, WACCM-X is free-running. While WACCM-X extends up to about 500–700 km altitude (145 levels), we only consider the altitude region relevant for infrasound propagation, which is up to 140 km altitude. The model has grid cells of 1.9° × 2.5° in latitude-longitude and a 3-hr temporal resolution (see the Data availability Section).

According to Garcia et al. (2017), WACCM incorporates three distinct types of GWs parameterizations. These include stationary waves created by orography-induced flow, as described by McFarlane (1987), convective-generated waves with a range of phase speeds, as detailed by Beres et al. (2005), and front-generated waves with a spectrum of phase speeds, as presented by Richter et al. (2010). As addressed by H.-L. Liu et al. (2018), the orographic and nonorographic GW forcing in SD-WACCM-X are parameterized following Garcia et al. (2017) and Richter et al. (2010) respectively. For a more detailed description of chemical and physical processes and parameterizations included in the model, see the studies by H.-L. Liu et al. (2018) and J. Liu et al. (2018).

The WACCM-X model has been validated against observations and empirical models and has shown a good agreement in thermospheric composition, density and tidal amplitudes (H.-L. Liu et al., 2018). The performance of the WACCM (and therefore WACCM-X) in representing the global dynamics of the MLT region is discussed and compared to observations in study by A. K. Smith (2012). The SD-WACCM-X model has been found to be representative of the Earth's atmosphere in studies of different atmospheric phenomena: for example, elevated-stratopause events (Orsolini et al., 2017; Siskind et al., 2021), dynamics (Kumari et al., 2021), and atmospheric tides (Pancheva et al., 2020; van Caspel et al., 2022; Zhang et al., 2021).

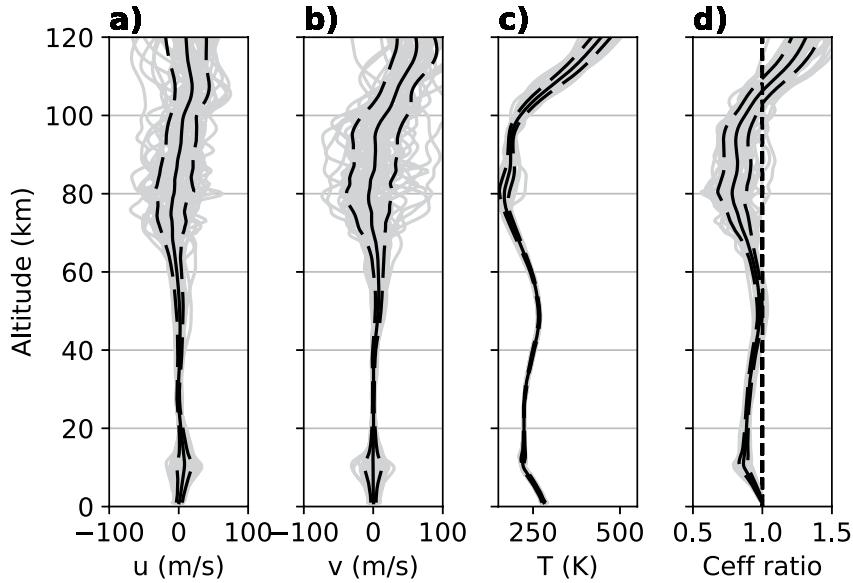

Figure 4. SD-WACCM-X atmospheric specifications for the 49 analyzed Hukkakero explosions, extracted at the grid point closest to the site around the time of the explosion. (a) zonal wind, (b) meridional wind, (c) temperature, (d) effective sound speed ratio.

In contrast to other models routinely used for infrasound propagation, SD-WACCM-X provides a single consistent atmospheric model covering the altitude region relevant for long-range infrasound propagation, with a suitable spatio-temporal resolution. In particular, WACCM-X should provide a more physical description of the MLT region when compared to atmospheric specifications that are typically used for thermospheric arrival modeling, such as the HWM/MSIS climatological models (Drob, 2019). Due to the proximity of the source to the receiver, the atmosphere can be approximated as a 1-D layered medium without time dependence. To avoid interpolation in space and time, we extract pressure, temperature, zonal and meridional winds from the grid node closest to the explosion site (Figure 1) and the time step closest to the explosion origin time.

The atmospheric conditions for all 49 Hukkakero events are presented in Figure 4. Zonal and meridional winds in the stratosphere (20–50 km) are weak and have absolute values of up to 18 m/s. Their variation from explosion to explosion is negligible with a standard deviation of 1–5 m/s. This can be explained by the summer-to-winter transition in the stratospheric polar vortex where zonal wind is reversing from westward summer circulation to eastward winter circulation (Waugh et al., 2017; Waugh & Polvani, 2010). In contrast, atmospheric winds in the mesosphere—lower thermosphere (50–120 km) reach values of up to 100 m/s and vary strongly between explosions (standard deviation of up to 33 m/s). Figure 4 also shows $C_{\text{eff}}(z)$ ratio profiles (see Section 3.1) that have been computed using the SD-WACCM-X model (see Section 2). It can be seen that around 50 km altitude the ratio is close but does not exceed unity for most profiles, except for the events on 13 and 14 August 2015 (days 225 and 226). This indicates that the presence of a strong stratospheric waveguide for the Hukkakero-IS37 configuration in late summer is rather rare and therefore (strong) stratospheric returns would not be expected at IS37. In contrast, the effective sound speed ratio exceeds unity around lower thermosphere in all cases. This can be attributed to the strong temperature gradient, which guarantees the presence of a thermospheric waveguide.

The effects of small-scale atmospheric fluctuations on stratospheric arrivals are particularly enhanced during periods of the year when the C_{eff} ratio near the stratopause is close to unity (Assink et al., 2014). Under these conditions, the small perturbations (e.g., GWs induced wind and temperature perturbations) can cause conditions favorable for (a) refraction or (b) reflection. The propagation effects (refraction or reflection) strongly depend on the vertical scale of the atmospheric fluctuations in comparison to the infrasonic wavelength. For relatively large vertical scales, refraction of infrasonic waves can be simulated with ray theory, showing variations in travel time and back-azimuth (Kulichkov, 2010). In contrast, infrasound scattering (or partial reflection) on vertical scales comparable to the infrasonic wavelength is a full-wave effect that cannot be simulated using ray theory. Indeed, several studies (Blixt et al., 2019; Chunchuzov & Kulichkov, 2020; Green et al., 2018) have reported observations

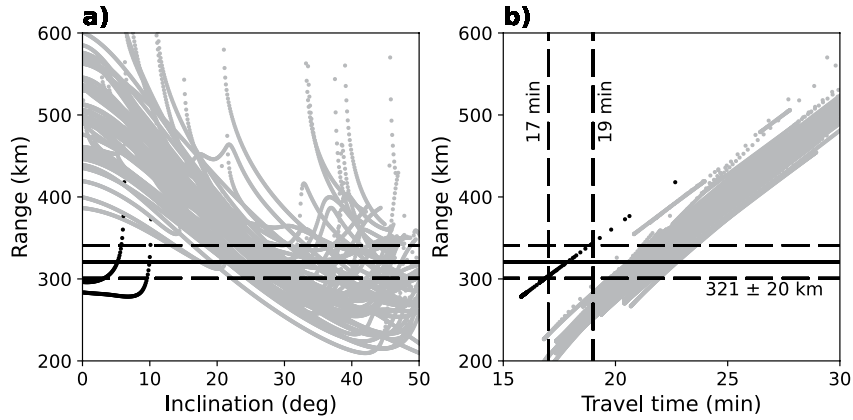

Figure 5. The first ground intercept information predicted by InfraGA for all explosive events. (a) Eigenray departure inclination vs. the distance from the source, (b) travel time versus distance from the source. The eigenray turning height is color coded (<60 km—black dots, ≥60 km—gray dots). The Hukkakero-IS37 great-circle distance and the tolerance distance interval considered for ground intercept are indicated as a solid black line and dashed black lines, respectively. Observed travel time of the first arrival at IS37 is between 17 and 19 min (dashed black lines).

of partial reflections from stratospheric altitudes in the region where no stratospheric rays are predicted (i.e., the shadow zone).

3.3. Ray-Tracing Using the SD-WACCM-X Model

For each of the analyzed Hukkakero events, we simulated infrasound propagation through its SD-WACCM-X atmospheric profile using the InfraGA ray tracer in 2-D Cartesian mode (see the Data availability Section for links and references). Rays were launched from the location of Hukkakero in the direction of IS37 with inclination angles ranging from 0° to 60° measured from the horizontal.

Figure 5a shows ray departure inclination angle against distance from Hukkakero for refracted paths predicted by ray theory. Almost all of the predictions correspond to thermospheric refracted paths with turning heights in the lower thermosphere, near ∼100 km (gray dots). As was mentioned before, these thermospheric arrivals are often observed at IS37 station Figure 3. Figure 5b shows the corresponding travel time (in min) for these rays. Stratospheric arrivals with arrival times between 17 and 19 min that correspond to our observations (Figure 3) are only predicted for two events that occurred on 13 and 14 August 2015 (days 225 and 226). It follows from analysis of the SD-WACCM-X profiles (Figure 4), that for these 2 days the $C_{\text{eff}}(z)$ ratio exceeds unity in the stratosphere.

From the ray-tracing simulations, it can be concluded that (a) IS37 is located in a stratospheric shadow zone (i.e., there is no refraction-supported stratospheric duct) for the vast majority of cases and (b) refracted infrasound reaches the station via thermospheric ducts. Therefore, it is presumed that the stratospheric signals arrive at IS37 station after being partially reflected in the middle atmosphere (Chunchuzov et al., 2011; Kulichkov, 2010).

Figure 6 illustrates the raypaths of a stratospheric and a thermospheric arrival at IS37 for the analyzed Hukkakero events. The $C_{\text{eff}}(z)$-ratio profile shown in the figure is computed based on the SD-WACCM-X model for 22 August 2017 at 12:00 UTC. The only arrival predicted by ray tracing is a thermospheric refracted ray that propagates up to 113 km and is predicted to arrive at IS37 after ∼22 min, which matches the observations (see Figure 3).

The reflected rays are not predicted by the classical ray theory but are instead constructed using a mirroring procedure akin to the approach in, for example, Blixt et al. (2019) and Green et al. (2018). We trace all rays until they reach the midpoint between Hukkakero and IS37 and then mirror them to continue the path back to the surface. Due to acoustic reciprocity, this is a valid approach in a range-independent medium. It is hypothesized that these rays have scattered from an atmospheric layer with small-scale fluctuations in wind and temperature. The travel time is then estimated as twice the propagation time to the midpoint. The altitudes of the lower and upper boundaries of the reflective layer (z_{bottom} and z_{top}) are defined from the two rays that best match the observed beginning and ending of the processed infrasound signal (t_{start} and t_{end}). In case of a large discrepancy between the predicted t_{start} and observed t_{start}, we first estimate z_{top} by matching predicted t_{end} to observations, and then obtain

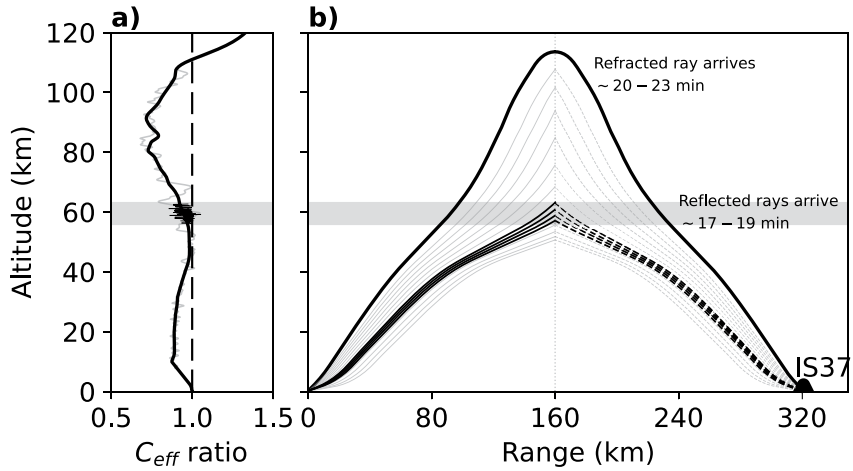

Figure 6. A schematic representation of infrasound raypaths from Hukkakero to IS37 relevant to this study. (a) Effective sound speed ratio in direction of IS37 with conceptual gravity wave perturbations (gray) and inhomogeneous layer of $C_{\text{eff}}(z)$ fluctuations (black). (b) Thermospheric ducting simulated by ray theory and explaining later arrivals (20–23 min) with U-shape (thick black line). Earlier arrivals (17–19 min) that are not predicted by ray theory can be explained by infrasound being scattered by small-scale $C_{\text{eff}}(z)$ fluctuations in an atmospheric layer (dashed black lines).

the lower boundary as $z_{\text{bottom}} = z_{\text{top}} - C_{\text{eff}}(t_{\text{end}} - t_{\text{start}})$. Here, the effective sound speed in the reflective layer is assumed to be constant.

3.4. Effective Sound Speed Retrieval

We applied the approach of Chunchuzov et al. (2015) to retrieve fine-scale effective sound-speed variations in the middle atmosphere. This method was designed to be applied to stratospheric and thermospheric arrivals in the shadow zone, assuming that infrasound was scattered from inhomogeneous atmospheric layers with fine-scale $C_{\text{eff}}(z)$ fluctuations. It was demonstrated in Chunchuzov et al. (2013) that temperature variations contribute relatively little to the effective sound-speed fluctuations (~20%) compared to wind variations (~80%). Therefore, we associate $C_{\text{eff}}(z)$ fluctuations with variations in horizontal wind.

This section presents the salient details behind the algorithm for the retrieval procedure, and provides a description of the main underlying assumptions. For a more detailed derivation of the equations and discussion of the method, we refer to Chunchuzov et al. (2015, 2022) and Chunchuzov and Kulichkov (2020). For convenience, most nomenclature and designations used in the current study are the same as in these original studies.

The fine-scale effective sound-speed inversion approach is based on:

(1) The assumption that infrasound is scattered or partially reflected at the midpoint between the source and receiver in a moving atmospheric layer with vertical fluctuations in the effective refractive index (see Chunchuzov et al., 2013, Equation 14),

$$\varepsilon(z) = -2(\Delta c + \Delta u \sin\theta_0)/\left(c_1 \cos^2\theta_0\right), \tag{2}$$

where Δc are the sound speed fluctuations; Δu is the projection of wind fluctuations on the source-receiver radius vector; c_1 is the average sound speed in the layer; and θ_0 is the angle of incidence on the layer at altitude z. The effective refractive index fluctuations, $\varepsilon(z)$, are assumed to be non-zero only inside the moving layer. A detailed derivation of Equation 2 is provided in Appendix of Chunchuzov et al. (2013).

(2) The relationship between the vertical profile of the effective refractive index fluctuations, $\varepsilon(z)$, and the scattered signal waveform, $p'(t)$, is (see Chunchuzov et al., 2013, Equation 21):

$$p'(t) = -\frac{p'_m r_0}{4R_1} \int_{-\infty}^{\infty} f(t - R_1/c_1 - z/a)\, \frac{d\varepsilon(z')}{dz'}\, \mathrm{d}z, \tag{3}$$

where p'_m is the peak signal amplitude recorded at distance r_0 close to the source; R_1 is the total distance along the propagation path; $f(t)$ is the normalized acoustic pressure waveform at r_0; $a = c_1/(2\cos\theta_0)$ is a coefficient representing the speed of the infrasound in the refractive layer; and $d\varepsilon(z)/dz$ is the spatial derivative of $\varepsilon(z)$. The dimensionless waveform of the scattered signal is defined as $I_0(t) = p'(t)R_1/(p'_m r_0)$.

(3) The assumption that the initial signal waveform, $f(t)$, has an N-wave shape (Lonzaga et al., 2015) near the source and a duration T_0 at the reflective layer altitude.

After integrating Equation 3 by parts and keeping in mind that function $\varepsilon(z)$ is defined only inside the moving layer, as well as that the derivative of N-wave has local maxima (more details in Chunchuzov and Kulichkov (2020)), the relation between the profile of effective refractive index fluctuations and the dimensionless waveform of the scattered signal becomes (see Chunchuzov et al., 2013, Equation 25)

$$I_0(t) = -\frac{\varepsilon\left(a\left[t - R_1/c_1\right]\right) + \varepsilon\left(a\left[t - R_1/c_1 - T_0\right]\right)}{4}. \quad (4)$$

The choice of the N-wave shape for the initial signal waveform, $f(t)$, is justified when the nonlinear effects are strong enough to form an N-wave when propagating the initial signal to the altitudes of reflection. In this case, transition between Equations 3 and 4 is valid. Otherwise, Equation 3 should be solved to find the function $\varepsilon(z)$. For example, if an incident signal has only one shock front at the head part of the signal, then only the first term in Equation 4 needs to be taken into account. This may happen in the lower troposphere, for example, when consider the partial reflection of acoustic signals in the stably-stratified boundary layer (Chunchuzov et al., 2017).

Equation 4 can be solved numerically for a set of discrete time samples with respect to $\varepsilon(z)$ using the method of least squares (see Appendix B for details). Next, the effective sound speed fluctuations, $\Delta C_{\text{eff}}(z)$, can be estimated from the $\varepsilon(z)$ profile using Equation 2 (Appendix B). However, several parameters need to be specified before solving Equation 4:

- The average sound speed c_1 is obtained by matching the travel time predicted by ray-tracing simulations to the observed travel time, and thereby determining the altitude range of the reflective layer and averaging the sound speed within it, as well as angle θ_0.
- An estimate of the peak overpressure close to the source, p'_m, is obtained using the model by Kinney and Graham (1985) based on the blast yield. The typical yield of Hukkakero explosions is presumed to be approximately 20 ton of TNT equivalent (Gibbons et al., 2015). According to the Kinney and Graham (1985) model with the initial conditions $W = 20$ ton TNT, $P_{\text{ref}} = 1.01325 \times 10^5$ Pa, and $\rho_{\text{ref}} = 1.225$ kg/m^3 (COESA, 1976), the peak overpressure at $r_0 = 1$ km from the source becomes $p'_m = 2320$ Pa.
- As the initially generated shock wave propagates, it experiences attenuation and becomes distorted due to non-linear propagation effects, which become more prominent with increasing height due to decreasing atmospheric density with altitude (Blom & Waxler, 2021; Lonzaga et al., 2015). One of the distortion features associated with non-linear propagation is period lengthening, which occurs since positive and negative phases of the pressure wave travel at slightly different speed (Hamilton & Blackstock, 2008). This contributes to decreasing the amplitude of the acoustic pulse as its duration increases following the acoustic-pulse conservation law (Kulichkov et al., 2017). To get an estimate of the N-wave duration at the reflective layer altitude, weakly non-linear propagation simulations were performed using InfraGA. Properties of the initially generated shock wave (peak overpressure of 2320 Pa and positive pressure phase of 0.11 s) were calculated based on the Kinney and Graham (1985) model described above. Values of T_0 in the range of 1–2 s were found to correspond to altitudes in the range of 50–80 km. This is the region from where we expect rays to reflect from, following the travel-time based mirroring simulations as described in Section 3.3.

4. Results

4.1. The Effective Sound-Speed Fluctuations Retrieved

This study analyzes the first (stratospheric) Hukkakero arrivals in the infrasound recordings described in Section 3.1 and illustrated in Figure 3. For each of the 49 Hukkakero blasts investigated, we processed a 30 s segment of the infrasound best-beam signal traces using the recipe provided in Section 3.4. Figure 7 displays the $\Delta C_{\text{eff}}(z)$ profiles retrieved. There is a day-to-day variability in the reflective layer altitude, with all $\Delta C_{\text{eff}}(z)$ profiles being located within stratopause–lower mesosphere altitudes of 50–75 km with the average depth of

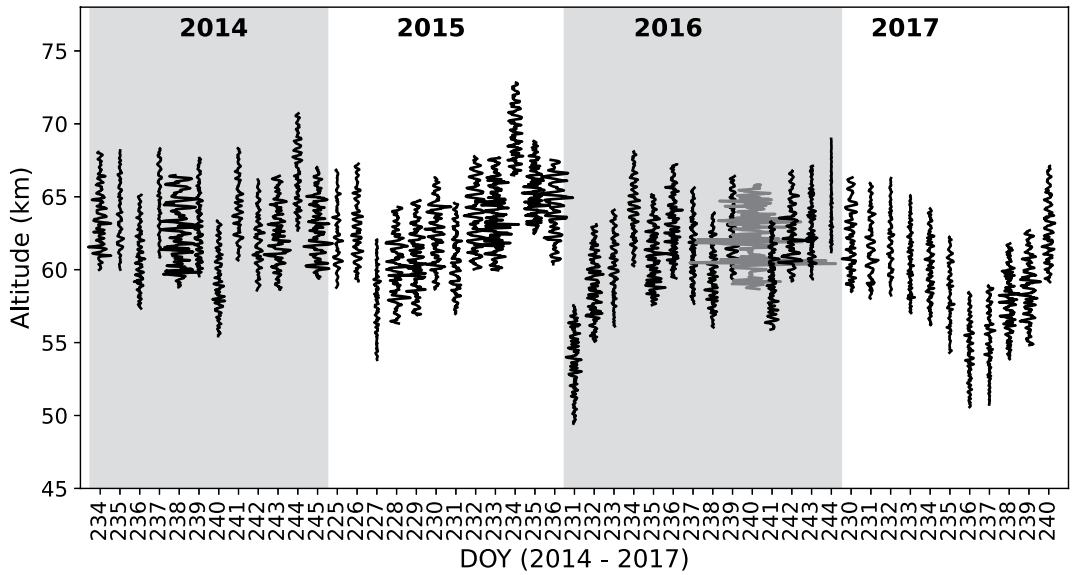

Figure 7. Retrieved fluctuations of the effective sound speed $C_{\text{eff}}(z)$. The $C_{\text{eff}}(z)$ profile on 27 August 2016 (day 240) with exceptionally high values (more details in the text) is displayed in gray to avoid overlapping with other profiles.

7.75 ± 0.38 km. Previous studies demonstrate that infrasound signal characteristics observed for events with similar strength and source-receiver geometry are highly sensitive to varying middle atmospheric winds and temperatures (Averbuch et al., 2022; Drob, 2019; Le Pichon et al., 2002). Therefore, the difference in the arrival time between events, as displayed in Figure 3, can be related to the variation in the infrasound probing altitude. This is confirmed by the overall agreement in the arrival time variations for the explosions studied and the associated altitude variation of the retrieved fluctuation profiles, see Figure 7. It should be noted that the same $\Delta C_{\text{eff}}(z)$ retrieval procedure can also be applied to later arrivals, which correspond to higher altitudes, as demonstrated in Chunchuzov et al. (2022).

The majority of the effective sound-speed fluctuations retrieved, $\Delta C_{\text{eff}}(z)$, have amplitudes of up to 5 m/s. However, for some cases, the amplitudes reach up to 15 m/s. Exceptionally high $\Delta C_{\text{eff}}(z)$ amplitudes of up to 25 m/s are estimated from the waveform recorded on 27 August 2016 (day 240 shown as the gray profile in Figure 7). There are two reasons behind it. First, the signal amplitude reaches 2 Pa which is larger than for any other event. Second, rapid changes in the waveform amplitude make it difficult for the fitting procedure to find an appropriate solution (see Appendix B). We consider this event as an outlier and suggest that it should be interpreted as a refracted rather than reflected arrival, and therefore remove it from the analysis. The root-mean-square error (RMSE) of $\Delta C_{\text{eff}}(z)$ retrieved varies within 6%–18% (see Appendix A). This RMSE is calculated based on the difference between the left- and right-hand sides of Equation 4 (see Appendix B for details).

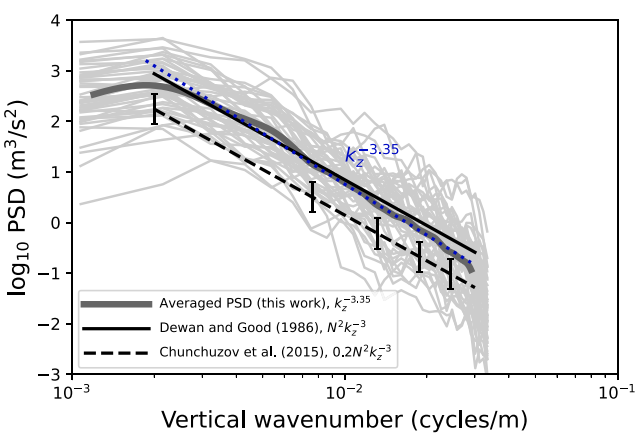

Figure 8. Vertical wavenumber power spectral density (PSD) of the retrieved $\Delta C_{\text{eff}}(z)$ fluctuations (light gray lines) and their mean (dark gray line) versus theoretical models by Dewan and Good (1986) (black solid) and Chunchuzov et al. (2015) (black dashed). Black error bars indicate variability in theoretical PSD amplitude based on other theories mentioned in the text. The blue dotted line indicates the power-law fitting region for the mean PSD.

Next, we perform a vertical wavenumber spectral analysis of the retrieved $\Delta C_{\text{eff}}(z)$ profiles by estimating the PSD using Welch's method (Welch, 1967) with a Hamming window (window length of 750 m or 50 samples and 50% overlap). Figure 8 displays the vertical wavenumber PSD of the retrieved effective sound-speed fluctuation profiles, as well as their mean. It can be seen that negative PSD slope is present for all events. The vertical wavenumber, k_z, that corresponds to the beginning of the negative slope is denoted the dominant wavenumber, m_*. Based on the analyzed events, $m_* = 2.15 \times 10^{-3} \pm 4.4 \times 10^{-4}$ cycles/m (see Appendix A). Fitting the k_z^p power-law within $k_z > m_*$ provides an estimate of $p = -3.35$ for the mean PSD and $p = -3.50 \pm 0.39$ for all profiles (see Appendix A).

The power-law exponents obtained in this study are within about 10% of −3. The k_z^{-3} power-law is known to correspond to the "universal" spectrum of horizontal wind fluctuations induced by GWs or GW saturation spectrum (Fritts & Alexander, 2003). The saturation spectrum amplitude was shown to correspond to $CN^2k_z^{-3}$ where N is the Brunt-Väisälä frequency, and C is a constant. The power-laws corresponding to linear (Dewan & Good, 1986) and non-linear (Chunchuzov et al., 2015) theoretical models of GW saturation ($C = 1$ and $C = 0.2$, respectively) are displayed in Figure 8 together with error bars indicating possible variability in theoretical PSD amplitude ($C = 0.1$–0.4; Hines, 1991). In both theoretical models, the altitude regime is controlled via the Brunt-Väisälä frequency, N. We use $N = 1.66 \times 10^{-2}$ rad/s in our calculations, which is typical for the lower mesosphere (Dewan & Good, 1986). From Figure 8 it is clear that the theoretical models show a good agreement with the mean spectrum of the retrieved $\Delta C_{\text{eff}}(z)$ profiles. For the chosen value of N (that controls amplitudes of the theoretical power-laws), the mean spectrum fits better to the theory by Dewan and Good (1986). However, the Brunt-Väisälä frequency in this altitude region may vary (e.g., Dewan & Good, 1986), and the most relevant theory would then change correspondingly. Therefore, it cannot be concluded which of the theories best explain the infrasound-based spectra. Instead, we say that the infrasound-based vertical wavenumber spectra are consistent with previously obtained theoretical spectra when taking into account the confidence intervals of those measurements (Fritts & Alexander, 2003).

From the spectral analysis, we can estimate the outer and inner vertical scale of atmospheric inhomogeneities that infrasound is sensitive to, based on the vertical wavenumber limits within which the k_z^{-3} power-law establishes. Denoting the highest vertical wavenumber as m_{end}, we obtain $L_{\text{inner}} = 1/m_{end} = 33$–$37$ m and $L_{\text{outer}} = 1/m_* = 386$–$585$ m. Note that the limited altitude range of the $\Delta C_{\text{eff}}(z)$ profiles retrieved restricts the sensitivity to motions with smaller vertical wavenumbers (larger vertical scales). This could be improved by processing longer segments of infrasound waveforms as was demonstrated in for example, Chunchuzov et al. (2013, 2015).

4.2. Comparison With the Saura MF Radar

As $C_{\text{eff}}(z)$ fluctuations are mostly associated with variations in horizontal wind (Section 3.4), it would be interesting to compare the vertical wavenumber spectra obtained in this study to spectra of wind measured by the Saura MF radar near the IS37 array (Figure 1). For this purpose, the spectral characteristics of 11 infrasound-based $\Delta C_{\text{eff}}(z)$ profile retrievals from 2017 were compared. First, we directly compare the Saura radar winds to the SD-WACCM-X model winds. As the effective sound speed $\Delta C_{\text{eff}}(z)$ is taken along the horizontal infrasound propagation direction (Equation 1), we project the Saura radar wind on the same unit vector pointing from Hukkakero toward IS37: $\mathbf{u} \cdot \hat{n} = u\sin(\phi) + v\cos(\phi)$, where ϕ is the Hukkakero-IS37 azimuth. The same projection was applied to the SD-WACCM-X wind profiles, extracted at the grid node located between the Saura radar and IS37 (Figure 1).

This comparison between Saura radar and SD-WACCM-X winds is displayed in Figures 9a and 9b. Although the radar measurements do not fully cover the altitude region where the infrasound-based $\Delta C_{\text{eff}}(z)$ profiles are retrieved (highlighted in Figures 9a and 9b), it can still be seen that the Saura wind measurement features a pattern similar to the SD-WACCM-X model. There is a weak wind pattern (<50 m/s) that alternates between positive and negative values, mostly modulated by tidal waves. Above 70 km, a noticeable discrepancy between measured and modeled winds is observed. This may be related to a lower temporal resolution of the model compared to the radar, the distance between the sampling locations, or to inaccuracies in the parametrization of GW breaking used in the SD-WACCM-X model (see Section 3.2.2). Moreover, note that above ∼50 km SD-WACCM-X is not supported by any observational data set and is, therefore, expected to deviate more from the measurements. This discrepancy between the radar measured winds and SD-WACCM was also shown in (de Wit et al., 2014), and is not unique to our measurements.

Next, we interpolate the SD-WACCM-X profiles to the radar vertical grid and perform a spectral comparison between the SD-WACCM-X and Saura radar wind profiles closest in time to the explosion onset. The obtained vertical wavenumber spectra are displayed in Figure 9c together with GW saturation theories from Figure 8. Note that the radar can only observe vertical variations at wavenumbers below approximately $k_z = 10^{-3}$ cycles/m due to its vertical resolution (Section 3.2.1). One can see a good agreement in PSD amplitudes between the radar, atmospheric model and GW saturation theories. However, it's clear that SD-WACCM-X wind spectra have steeper slope and seem to underestimate amplitudes at ranges 10^{-4}–10^{-3} cycles/m. A more detailed look into SD-WACCM-X and Saura radar horizontal winds over long time periods is needed to fully understand the

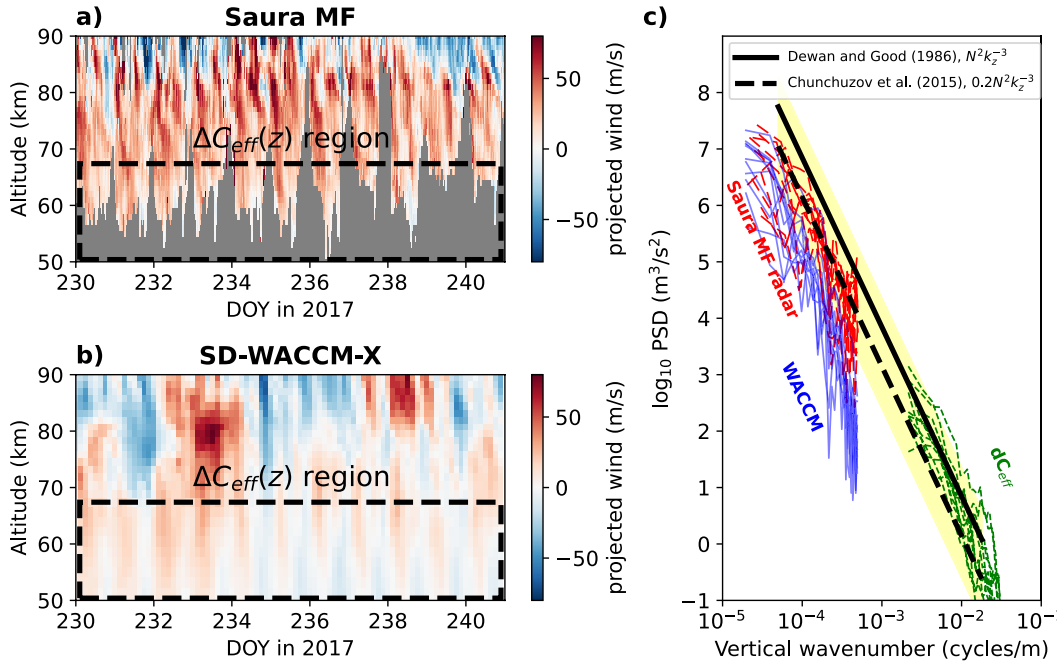

Figure 9. (a) Projection of wind measured by Saura MF radar and (b) predicted by SD-WACCM-X on the vector connecting Hukkakero and IS37. (c) Vertical wavenumber spectra of the Saura radar winds (red dashed), SD-WACCM-X winds (blue solid) and retrieved $\Delta C_{\text{eff}}(z)$ fluctuations (green dotted) for the explosions in 2017, versus theoretical models by Dewan and Good (1986) (black solid) and Chunchuzov et al. (2015) (black dashed). Yellow shade illustrates possible variations in the saturation spectrum amplitude for different values of the constant C and the Brunt-Väisälä frequency N (see text for more details).

nature of such discrepancy. We leave this question open for further research suggesting that parametrization of subgrid-scale processes in SD-WACCM-X can probably be improved.

To resolve the high-wavenumber part of the spectrum that the Saura radar and SD-WACCM-X are insensitive to due to their vertical resolution, the $\Delta C_{\text{eff}}(z)$ profiles retrieved are used. The vertical wavenumber spectra for the $\Delta C_{\text{eff}}(z)$ profiles in 2017 are presented in Figure 9c. As was shown earlier (Figure 8), the high-wavenumber part of the spectrum follows the k_z^{-3} power-law and agrees well in amplitude with linear and non-linear GW saturation theories. However, we acknowledge that there is a difference in power-laws that radar-retrieved and infrasound-retrieved PSDs follow in Figure 9c. Looking at the radar and infrasound data in the context of the k_z^{-3} power-laws by Chunchuzov et al. (2015) and Dewan and Good (1986), we note that the amplitudes of the infrasound-retrieved spectra follow more closely the Dewan and Good (1986) model, while the radar wind spectra are closer to the Chunchuzov et al. (2015) model. It can again be noted that these power laws both include the N^2 factor and that there is uncertainty in the value of the Brunt-Väisälä frequency depending on the altitude. In the altitude regime of consideration (50–90 km), this number can vary approximately between $N = 1.66 \times 10^{-2}$ rad/s (for upper stratosphere—lower mesosphere) and $N = 2.2 \times 10^{-2}$ rad/s (for upper mesosphere—lower thermosphere), which will translate to N^2 factors between 2.74×10^{-4} and 4.86×10^{-4} based on the (COESA, 1976). Overall, the results obtained allow us to suggest that Saura radar and infrasound-based $\Delta C_{\text{eff}}(z)$ profiles represent low- and high-wavenumber parts of the same "universal" GW spectrum.

5. Discussion

The current study applies the effective sound-speed retrieval procedure by Chunchuzov et al. (2015) to infrasound recordings in the shadow zone. This is the first time the aforementioned approach is applied to a large and consistent data set. Because $\Delta C_{\text{eff}}(z)$ profiles are retrieved along a fixed source-receiver path and because the explosion yields are similar for each event, we can consider the variability in the infrasound recordings as being related to atmospheric dynamics.

The results show that vertical wavenumber PSDs obtained from the $\Delta C_{\text{eff}}(z)$ profiles are close to the "universal" GW saturation spectrum of k_z^{-3}. Various theories were proposed to explain the dynamics behind GW saturation, that is, instability and wave-wave interaction. C typically has values within 0.1–0.4 (Hines, 1991) depending on the theory and assumptions made. The first attempt to describe universality in measured wind spectra (e.g., Dewan et al., 1984; Endlich et al., 1969) was made by Dewan and Good (1986) who assumed saturation via convective instabilities at each vertical wave number independently and yielded $C = 1$. Later, this theory was extended by S. A. Smith et al. (1987) to account also for amplitude limiting instabilities arising from the whole wave spectrum instead, and value of $C = 1/6$ was obtained. These traditional linear saturation theories were criticized in Chunchuzov (2002) and Hines (1991), where it was shown that small-scale anisotropic inhomogeneities with k_z^{-3} vertical wavenumber spectrum are shaped due to non-resonant internal wave-wave interactions. Chunchuzov et al. (2015) compared vertical wavenumber spectra of effective sound-speed fluctuations retrieved from infrasound detections of five volcanic eruptions and one explosion. Based on this analysis, a value of $C = 0.2$ for the upper stratosphere was proposed. More insight on the history of the GW saturation theories and their developments is provided in (Fritts & Alexander, 2003).

The very end of the vertical wavenumber spectra in Figure 8 corresponds to motions at scales of tens of meters. This is on the edge of transition from the GW saturation regime to the turbulence regime where the theory predicts a transition from a k_z^{-3} power-law to $k_z^{-5/3}$ (e.g., Gardner et al., 1993). The vertical wavenumber where this transition occurs may have different values based on the latitude and altitude of interest, for example, the value of 2×10^{-3} cycles/m was proposed in Gardner et al. (1993) for mid-latitude mesopause region. In contrast, Endlich et al. (1969) analyzed vertical wind profiles measured during different seasons and found that their PSDs follow the k_z^{-3} power-law up to the vertical wavenumber of 10^{-2} cycles/m. Despite the $k_z^{-5/3}$ power-law is not observed in the infrasound-based spectra, we cannot admit not to acknowledge the possible limitations related to the approach introduced in Section 3.4 and the fact that the turbulence can be also observed at such high wavenumbers. This question could be addressed when comparing the effective sound-speed fluctuations to measurement techniques that have high vertical resolution and are sensitive to turbulence, for example, lidar. We leave this question open for future research.

Figure 9 clearly shows that the SD-WACCM-X wind underestimates the variability in the 70–90 km range for chosen days and shows rather a patchy pattern. It could be due to for example, subgrid-scale processes that include breaking primary GWs and their interactions with other waves as well as unresolved secondary GWs that can have a significant impact in the MLT region (Vadas & Becker, 2018). Unfortunately, these processes is something largely overlooked by current parameterizations. Another likely reason for the biases are quite different observational volumes and temporal resolutions of radar observations and global models like WACCM-X, which may result in the aforementioned biases. In addition, mesospheric winds in the SD-WACCM-X model may be influenced by uncertainties in the input data used to initialize the model. A more detailed comparison between the SD-WACCM-X and Saura radar is needed to better understand the nature of the differences in their representations of mesospheric winds.

In the present study, it is assumed that the stratospheric arrivals in the shadow zone are associated with partial reflections. However, it is important to note that the stratospheric arrival waveform could also be explained by other mechanisms that involve small-scale structures (e.g., Lalande & Waxler, 2016). In the presence of a weak stratospheric duct, small-scale structure can, for example, diffract the acoustic signal as shown by Popov et al. (2022) on example of the 4 August 2020 Beirut explosion. Alternatively, in the case of a "borderline stratospheric duct" (with the effective sound speed ratio is lower than but close to one), the small-scale structure can effectively fill the gap and produce a classical duct. For both mechanisms a "classical" ground-to-ground ray would exist between the source and receiver, and this would suggest that the effective sound speed at the turning height of the ray would be equal to the observed apparent velocity of the arrival. This is not the case for partially reflected rays where the apparent velocity could still be inferred from the inclination angle. It remains to be seen if those values would be much different, and we leave this question for future studies.

Possible avenues for future research can also include application of the same effective sound-speed retrieval approach to later mesospheric and thermospheric arrivals observed at IS37 (Figure 3). This would provide an opportunity to study thicker atmospheric layers and to possibly look at other physical phenomena that could be responsible for infrasound scattering (e.g., polar mesospheric summer echoes). Another possible direction of research could be comparing the effective sound-speed fluctuations obtained in this study to other measurement

techniques with high vertical resolution, for example, lidar. Moreover, studying the 3D wind and temperature fluctuations caused by GWs could be performed by applying the retrieval approach to several infrasound stations around the Hukkakero explosion site for example, ARCES/ARCI (Karasjok, Norway), KRIS (Kiruna, Norway) and APA/APAI (Apatity, Russia) (Gibbons et al., 2015).

6. Summary

In this study, infrasound waves from 49 blasts between 2014 and 2017 are used to retrieve effective sound speed fluctuations, $\Delta C_{\text{eff}}(z)$, in the middle atmosphere. The applied retrieval recipe is based on approaches previously developed by Chunchuzov et al. (2013, 2015). It is based on a relation between the waveform of the scattered infrasound signal recorded on the surface in the shadow zone and the $C_{\text{eff}}(z)$ fluctuation profile in an inhomogeneous atmospheric layer. The results obtained demonstrate that the infrasound scattering occurs in the lower mesosphere between 50 and 75 km altitude. This atmospheric region is also known to be altitudes where GWs start to break (Garcia & Solomon, 1985). Therefore, information about the $\Delta C_{\text{eff}}(z)$ retrieved from ground-based infrasound measurements is of direct interest for studying the GW activity and for potential improvement of GW parameterization schemes used in NWPs. The spectral analysis of retrieved effective sound speed fluctuations in terms of vertical wavenumber spectra revealed that the tail of the mean spectrum follows a k_z^{-3} power law. This law corresponds to the "universal" spectrum of horizontal wind fluctuations induced by GWs (Fritts & Alexander, 2003). The spectral characteristics of the 11 infrasound-based $\Delta C_{\text{eff}}(z)$ profiles retrieved for 2017 were compared against independent wind measurements by the Saura MF radar. Good agreement in amplitudes and slopes of the spectra was demonstrated, indicating that the infrasound and the radar measurements represent the high- and low-wavenumber sections of the "universal" gravity-wave spectrum, respectively. Therefore, the current study opens the way for the remote sensing of GW activity by means of ground-based infrasound measurements and to improve the representation of small-scale wind inhomogeneities in upper atmospheric model products. The latter would be beneficial for the infrasound scientific field since advanced simulations of infrasound propagation require atmospheric specifications with high vertical resolution (Chunchuzov et al., 2015; Hedlin & Drob, 2014; Lalande & Waxler, 2016; Sabatini et al., 2019). The prospects of using explosive event sequences as *data sets of opportunity* for the middle atmospheric remote sensing can pave the way for an enhanced GW representation in atmospheric models.

Appendix A: Retrieved Parameters and Comparisons

Table A1 provides details about the spectral analysis performed in Section 4.

Table A1
Explosion Origin Time, Dominant Wavenumber and the Slope for the Corresponding Spectrum

Origin time (yyyy-mm-dd HH:MM:SS, UTC)	DOY	m_* [cycl/m]	Exponent in k_z^p	RMSE relative to max amplitude
2014-08-22 11:59:59	234	2.15e−3	−3.79	0.06
2014-08-23 10:29:59	235	1.07e−3	−3.43	0.08
2014-08-24 11:59:59	236	2.15e−3	−3.29	0.13
2014-08-25 10:29:59	237	1.07e−3	−3.23	0.10
2014-08-26 10:59:59	238	2.15e−3	−3.04	0.07
2014-08-27 10:59:59	239	2.15e−3	−2.95	0.08
2014-08-28 10:59:59	240	2.15e−3	−3.30	0.08
2014-08-29 10:29:59	241	2.15e−3	−3.83	0.13
2014-08-30 10:29:59	242	2.15e−3	−3.95	0.10
2014-08-31 10:59:59	243	2.15e−3	−3.63	0.08
2014-09-01 09:59:59	244	2.15e−3	−3.67	0.13
2014-09-02 09:29:59	245	2.15e−3	−3.25	0.09
2015-08-13 10:59:59	225	2.15e−3	−3.71	0.08
2015-08-14 10:04:59	226	2.15e−3	−3.54	0.14

Table A1
Continued

Origin time (yyyy-mm-dd HH:MM:SS, UTC)	DOY	m_* [cycl/m]	Exponent in k_z^p	RMSE relative to max amplitude
2015-08-15 10:59:59	227	2.15e−3	−3.87	0.09
2015-08-16 10:59:59	228	2.15e−3	−3.56	0.09
2015-08-17 11:59:59	229	2.15e−3	−3.02	0.13
2015-08-18 09:59:59	230	2.15e−3	−3.86	0.06
2015-08-19 09:29:59	231	2.15e−3	−2.90	0.08
2015-08-20 09:29:59	232	2.15e−3	−3.57	0.13
2015-08-21 09:29:59	233	2.15e−3	−3.19	0.08
2015-08-22 11:29:59	234	2.15e−3	−2.84	0.11
2015-08-23 11:29:59	235	2.15e−3	−2.65	0.09
2015-08-24 12:00:00	236	2.15e−3	−3.52	0.06
2016-08-18 12:29:59	231	2.15e−3	−3.18	0.10
2016-08-19 11:29:59	232	2.15e−3	−4.00	0.12
2016-08-20 13:29:59	233	2.15e−3	−3.76	0.07
2016-08-21 13:00:00	234	2.15e−3	−3.71	0.12
2016-08-22 11:59:59	235	2.15e−3	−3.60	0.09
2016-08-23 12:59:59	236	1.07e−3	−2.78	0.18
2016-08-24 11:59:59	237	2.15e−3	−3.06	0.12
2016-08-25 11:29:59	238	3.23e−3	−4.11	0.10
2016-08-26 11:29:59	239	2.15e−3	−3.36	0.10
2016-08-27 12:59:59	240	3.23e−3	−4.07	0.06
2016-08-28 10:59:59	241	2.15e−3	−3.13	0.13
2016-08-29 09:59:59	242	2.15e−3	−3.46	0.10
2016-08-30 07:54:59	243	3.22e−3	−3.13	0.07
2016-08-31 08:49:59	244	3.23e−3	−3.80	0.06
2017-08-18 11:59:59	230	2.15e−3	−4.25	0.18
2017-08-19 11:00:00	231	1.08e−3	−3.46	0.16
2017-08-20 12:00:00	232	2.15e−3	−3.70	0.08
2017-08-21 12:59:59	233	3.22e−3	−4.23	0.07
2017-08-22 11:59:59	234	2.15e−3	−3.47	0.10
2017-08-23 11:29:59	235	2.15e−3	−4.11	0.07
2017-08-24 11:29:59	236	2.15e−3	−4.06	0.14
2017-08-25 09:59:59	237	2.15e−3	−3.75	0.10
2017-08-26 10:59:59	238	2.15e−3	−3.59	0.07
2017-08-27 11:29:59	239	2.15e−3	−3.34	0.08
2017-08-28 10:29:59	240	2.15e−3	−3.40	0.11
	Mean	2.15e−3	−3.50	
	STD	4.40e−4	−0.39	

Appendix B: System of Equations to Solve Equation 4

In this section, we provide the same explanation on how to numerically solve Equation 4 as presented in Chunchuzov and Kulichkov (2020), but complemented with more detail.

Equation 4 represents the dimensionless waveform of scattered signal as a sum of two profiles of effective refractive index fluctuations shifted in time by the time interval T_0. Let us denote values of the scattered signal at

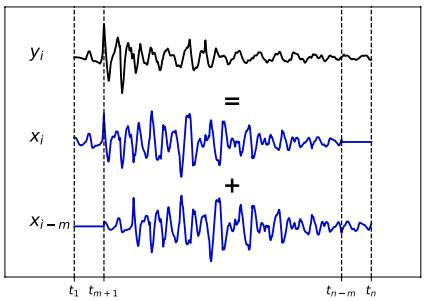

Figure B1. A synthetic example of Equation 4.

discrete times t_i as $y_i = I_0(t_i)$ where $i = 1, 2, \ldots, n$ (n is the number of samples), and effective refractive index fluctuations as $x_i = -\varepsilon(a[t_i - R_1/c_1])/4$ with non-zero values at $i = 1, 2, \ldots, n - m$ and $x_{i-m} = -\varepsilon(a[t_i - R_1/c_1 - T_0])/4$ with non-zero values at $i = m + 1, \mathrm{m} + 2, \ldots, n$, where m is the number of t_i values within the time interval T_0. Figure B1 demonstrates Equation 4 with the notation introduced.

Thus, the following system of linear algebraic equations with respect to x_i can be obtained from Equation 4:

$$\begin{cases} y_i = x_i, & \text{for } 1 \le i \le m \\ y_i = x_i + x_{i-m}, & \text{for } m + 1 \le i \le n - m \\ y_i = x_{i-m}, & \text{for } n - m + 1 \le i \le n. \end{cases} \tag{B1}$$

The number of unknowns in the system B1, $n - m$, is less than the number of equations, n, and the system is therefore overdetermined. In this case, the least squares method can be used to find an approximate solution by minimizing the difference $|\alpha X - Y|$ where $X = \{x_j\}$, $j = 1, 2, \ldots, n - m$, $Y = \{y_i\}$, $i = 1, 2, \ldots, n$, and α is a coefficient matrix of dimension $n \times (n - m)$.

After the solution has been found, the profile of the effective refractive index fluctuations can be retrieved as $\varepsilon(a[t_i - R_1/c_1]) = -4x_i$. Next, the effective sound fluctuation profile is obtained from $\varepsilon(z_i)$ values using Equation 2 as:

$$\Delta C_{\mathrm{eff}}(z_i) \approx \Delta c(z_i) + \Delta u(z_i)\sin\theta_0 = -\frac{\varepsilon(z_i)c_1\cos^2\theta_0}{2} = 2x_i c_1 \cos^2\theta_0. \tag{B2}$$

where $z_i = a(t_i - R_1/c_1)$ according to Chunchuzov et al. (2013). This formula was obtained under assumption that the speed of infrasound wave is constant up to the altitudes of scattering, and can therefore provide big errors when calculating the altitudes. For this reason, the actual mapping of travel time against altitude is performed using the ray-tracing based mirroring procedure in this study (Section 3.3).

Data Availability Statement

The 3-hourly SD-WACCM-X model product data are available via https://www.earthsystemgrid.org/dataset/ucar.cgd.ccsm4.SD-WACCM-X_v2.1.atm.hist.3hourly_inst.html (UCAR/NCAR, 2019). The InfraGA infrasound propagation code (e.g., Blom & Waxler, 2017; Blom & Waxler, 2021) is provided under open access on GitHub https://github.com/LANL-Seismoacoustics/infraGA (LANL, 2014). The IS37 infrasound station is part of the International Monitoring System (IMS) of the Preparatory Commission for the Comprehensive Nuclear-Test-Ban Treaty Organization (CTBTO). Data access can be granted to third parties and researchers through the virtual Data Exploitation Centre (vDEC) of the International Data Center: https://www.ctbto.org/specials/vdec/. The data set of Saura wind measurements used in this study is available at IAP (2023). More data can be obtained by contacting Toralf Renkwitz.

Acknowledgments
This research was supported by the Research Council of Norway FRIPRO/FRINATEK basic research program, project contract 274377: *Middle Atmosphere Dynamics: Exploiting Infrasound Using a Multidisciplinary Approach at High Latitudes* (MADEIRA). This work was partially supported by the Research Council of Norway under contract 223252/F50 and RSF Grant 21-17-00021. This study was facilitated by previous research performed within the framework of the ARISE and ARISE2 projects (Blanc et al., 2018, 2019), funded by the European Commission FP7 and Horizon 2020 programmes (Grants 284387 and 653980). The authors would also like to thank Yvan Orsolini for useful discussions and suggestions. In addition, the authors would like to thank two reviewers for careful reading the manuscript and providing their feedback that improved the quality of this article.

References

Amezcua, J., & Barton, Z. (2021). Assimilating atmospheric infrasound data to constrain atmospheric winds in a two-dimensional grid. *Quarterly Journal of the Royal Meteorological Society*, *147*(740), 3530–3554. https://doi.org/10.1002/qj.4141

Amezcua, J., Näsholm, S. P., Blixt, E. M., & Charlton-Perez, A. J. (2020). Assimilation of atmospheric infrasound data to constrain tropospheric and stratospheric winds. *Quarterly Journal of the Royal Meteorological Society*, *146*(731), 2634–2653. https://doi.org/10.1002/qj.3809

Assink, J., Le Pichon, A., Blanc, E., Kallel, M., & Khemiri, L. (2014). Evaluation of wind and temperature profiles from ECMWF analysis on two hemispheres using volcanic infrasound. *Journal of Geophysical Research: Atmospheres*, *119*(14), 8659–8683. https://doi.org/10.1002/2014JD021632

Assink, J., Smets, P., Marcillo, O., Weemstra, C., Lalande, J.-M., Waxler, R., & Evers, L. (2019). Advances in infrasonic remote sensing methods. In *Infrasound monitoring for atmospheric studies* (pp. 605–632). Springer. https://doi.org/10.1007/978-3-319-75140-5_18

Assink, J., Waxler, R., & Drob, D. (2012). On the sensitivity of infrasonic traveltimes in the equatorial region to the atmospheric tides. *Journal of Geophysical Research*, *117*(D1). https://doi.org/10.1029/2011JD016107

Assink, J., Waxler, R., Frazier, W., & Lonzaga, J. (2013). The estimation of upper atmospheric wind model updates from infrasound data. *Journal of Geophysical Research: Atmospheres*, *118*(19), 10707–10724. https://doi.org/10.1002/jgrd.50833

Averbuch, G., Ronac-Giannone, M., Arrowsmith, S., & Anderson, J. (2022). Evidence for short temporal atmospheric variations observed by infrasonic signals: 1. The troposphere. *Earth and Space Science*, *9*(3), e2021EA002036. https://doi.org/10.1029/2021EA002036

Bauer, P., Thorpe, A., & Brunet, G. (2015). The quiet revolution of numerical weather prediction. *Nature*, *525*(7567), 47–55. https://doi.org/10.1038/nature14956

Becker, E., Vadas, S. L., Bossert, K., Harvey, V. L., Zülicke, C., & Hoffmann, L. (2022). A high-resolution whole-atmosphere model with resolved gravity waves and specified large-scale dynamics in the troposphere and stratosphere. *Journal of Geophysical Research: Atmospheres*, *127*(2), e2021JD035018. https://doi.org/10.1029/2021JD035018

Bengtsson, L., Andrae, U., Aspelien, T., Batrak, Y., Calvo, J., de Rooy, W., et al. (2017). The HARMONIE–AROME model configuration in the ALADIN–HIRLAM NWP system. *Monthly Weather Review*, *145*(5), 1919–1935. https://doi.org/10.1175/MWR-D-16-0417.1

Beres, J. H., Garcia, R. R., Boville, B. A., & Sassi, F. (2005). Implementation of a gravity wave source spectrum parameterization dependent on the properties of convection in the whole atmosphere community climate model (WACCM). *Journal of Geophysical Research*, *110*(D10), D10108. https://doi.org/10.1029/2004JD005504

Bertin, M., Millet, C., & Bouche, D. (2014). A low-order reduced model for the long range propagation of infrasounds in the atmosphere. *The Journal of the Acoustical Society of America*, *136*(1), 37–52. https://doi.org/10.1121/1.4883388

Blanc, E., Ceranna, L., Hauchecorne, A., Charlton-Perez, A., Marchetti, E., Evers, L., et al. (2018). Toward an improved representation of middle atmospheric dynamics thanks to the ARISE project. *Surveys in Geophysics*, *39*(2), 171–225. https://doi.org/10.1007/s10712-017-9444-0

Blanc, E., Pol, K., Le Pichon, A., Hauchecorne, A., Keckhut, P., Baumgarten, G., et al. (2019). Middle atmosphere variability and model uncertainties as investigated in the framework of the ARISE project. In *Infrasound monitoring for atmospheric studies* (pp. 845–887). Springer. https://doi.org/10.1007/978-3-319-75140-5_28

Blixt, E. M., Näsholm, S. P., Gibbons, S. J., Evers, L. G., Charlton-Perez, A. J., Orsolini, Y. J., & Kværna, T. (2019). Estimating tropospheric and stratospheric winds using infrasound from explosions. *The Journal of the Acoustical Society of America*, *146*(2), 973–982. https://doi.org/10.1121/1.5120183

Blom, P., & Waxler, R. (2017). Modeling and observations of an elevated, moving infrasonic source: Eigenray methods. *The Journal of the Acoustical Society of America*, *141*(4), 2681–2692. https://doi.org/10.1121/1.4980096

Blom, P., & Waxler, R. (2021). Characteristics of thermospheric infrasound predicted using ray tracing and weakly non-linear waveform analyses. *The Journal of the Acoustical Society of America*, *149*(5), 3174–3188. https://doi.org/10.1121/10.0004949

Bossert, K., Fritts, D. C., Pautet, P.-D., Williams, B. P., Taylor, M. J., Kaifler, B., et al. (2015). Momentum flux estimates accompanying multiscale gravity waves over Mount Cook, New Zealand, on 13 July 2014 during the DEEPWAVE campaign. *Journal of Geophysical Research: Atmospheres*, *120*(18), 9323–9337. https://doi.org/10.1002/2015JD023197

Brekhovskikh, L. (1960). Propagation of acoustic and infrared waves in natural waveguides over long distances. *Soviet Physics - Uspekhi*, *3*(1), 159–166. https://doi.org/10.1070/PU1960v003n01ABEH003263

Brissaud, Q., Näsholm, S. P., Turquet, A., & Le Pichon, A. (2023). Predicting infrasound transmission loss using deep learning. *Geophysical Journal International*, *232*(1), 274–286. https://doi.org/10.1093/gji/ggac307

Chunchuzov, I. (2002). On the high-wavenumber form of the Eulerian internal wave spectrum in the atmosphere. *Journal of the Atmospheric Sciences*, *59*(10), 1753–1774. https://doi.org/10.1175/1520-0469(2002)059⟨1753:OTHWFO⟩2.0.CO;2

Chunchuzov, I., & Kulichkov, S. (2020). *Infrasound propagation in an anisotropic fluctuating atmosphere*. Cambridge Scholars Publishing.

Chunchuzov, I., Kulichkov, S., & Firstov, P. (2013). On acoustic N-wave reflections from atmospheric layered inhomogeneities. *Izvestiya, Atmospheric and Oceanic Physics*, *49*(3), 258–270. https://doi.org/10.1134/S0001433813020060

Chunchuzov, I., Kulichkov, S., Perepelkin, V., Popov, O., Firstov, P., Assink, J., & Marchetti, E. (2015). Study of the wind velocity-layered structure in the stratosphere, mesosphere, and lower thermosphere by using infrasound probing of the atmosphere. *Journal of Geophysical Research: Atmospheres*, *120*(17), 8828–8840. https://doi.org/10.1002/2015JD023276

Chunchuzov, I., Kulichkov, S., Popov, O., & Perepelkin, V. (2022). Infrasound propagation through the atmosphere with mesoscale wind velocity and temperature fluctuations. *Waves in Random and Complex Media*, 1–16. https://doi.org/10.1080/17455030.2022.2056259

Chunchuzov, I., Kulichkov, S., Popov, O., Waxler, R., & Assink, J. (2011). Scattering of infrasound by anisotropic inhomogeneities of the atmosphere. *Izvestiya - Atmospheric and Oceanic Physics*, *47*(5), 540–547. https://doi.org/10.1134/s0001433811050045

Chunchuzov, I., Perepelkin, V., Popov, O., Kulichkov, S., Vardanyan, A., Ayvazyan, G., & Khachikyan, K. Z. (2017). Studying characteristics of a fine layered structure of the lower troposphere on the basis of acoustic pulse sounding. *Izvestiya, Atmospheric and Oceanic Physics*, *53*(3), 279–293. https://doi.org/10.1134/S0001433817030045

COESA. (1976). *US standard atmosphere*. National Oceanic and Atmospheric Administration.

Cugnet, D., de la Camara, A., Lott, F., Millet, C., & Ribstein, B. (2019). Non-orographic gravity waves: Representation in climate models and effects on infrasound. In A. Le Pichon, E. Blanc, & A. Hauchecorne (Eds.), *Infrasound monitoring for atmospheric studies: Challenges in middle atmosphere dynamics and societal benefits* (pp. 827–844). Springer. https://doi.org/10.1007/978-3-319-75140-5_27

De Carlo, M., Ardhuin, F., & Le Pichon, A. (2020). Atmospheric infrasound generation by ocean waves in finite depth: Unified theory and application to radiation patterns. *Geophysical Journal International*, *221*(1), 569–585. https://doi.org/10.1093/gji/ggaa015

Dewan, E., & Good, R. (1986). Saturation and the "universal" spectrum for vertical profiles of horizontal scalar winds in the atmosphere. *Journal of Geophysical Research*, *91*(D2), 2742–2748. https://doi.org/10.1029/JD091iD02p02742

Dewan, E., Grossbard, N., Quesada, A., & Good, R. (1984). Spectral analysis of 10m resolution scalar velocity profiles in the stratosphere. *Geophysical research letters*, *11*(1), 80–83. https://doi.org/10.1029/GL011i001p00080

de Wit, R. J., Hibbins, R. E., Espy, P. J., Orsolini, Y. J., Limpasuvan, V., & Kinnison, D. E. (2014). Observations of gravity wave forcing of the mesopause region during the January 2013 major sudden stratospheric warming. *Geophysical Research Letters*, *41*(13), 4745–4752. https://doi.org/10.1002/2014GL060501

Diamond, M. (1963). Sound channels in the atmosphere. *Journal of Geophysical Research*, *68*(11), 3459–3464. https://doi.org/10.1029/JZ068i011p03459

Drob, D. (2019). Meteorology, climatology, and upper atmospheric composition for infrasound propagation modeling. In *Infrasound monitoring for atmospheric studies* (pp. 485–508). Springer. https://doi.org/10.1007/978-3-319-75140-5_14

Drob, D., Broutman, D., Hedlin, M., Winslow, N., & Gibson, R. (2013). A method for specifying atmospheric gravity wavefields for long-range infrasound propagation calculations. *Journal of Geophysical Research: Atmospheres*, *118*(10), 3933–3943. https://doi.org/10.1029/2012JD018077

Endlich, R. M., Singleton, R. C., & Kaufman, J. W. (1969). Spectral analysis of detailed vertical wind speed profiles. *Journal of Atmospheric Sciences*, *26*(5), 1030–1041. https://doi.org/10.1175/1520-0469(1969)026⟨1030:SAODVW⟩2.0.CO;2

Evers, L. G. (2008). *The inaudible symphony: On the detection and source identification of atmospheric infrasound* (PhD thesis). Delft University of Technology.

Fee, D., Waxler, R., Assink, J., Gitterman, Y., Given, J., Coyne, J., et al. (2013). Overview of the 2009 and 2011 Sayarim infrasound calibration experiments. *Journal of Geophysical Research: Atmospheres*, *118*(12), 6122–6143. https://doi.org/10.1002/jgrd.50398

Fritts, D. C., & Alexander, M. J. (2003). Gravity wave dynamics and effects in the middle atmosphere. *Reviews of Geophysics*, *41*(1). https://doi.org/10.1029/2001RG000106

Garcia, R. R., & Boville, B. A. (1994). "Downward control" of the mean meridional circulation and temperature distribution of the polar winter stratosphere. *Journal of Atmospheric Sciences*, *51*(15), 2238–2245. https://doi.org/10.1175/1520-0469(1994)051⟨2238:COTMMC⟩2.0.CO;2

Garcia, R. R., Smith, A. K., Kinnison, D. E., de la Cámara, Á., & Murphy, D. J. (2017). Modification of the gravity wave parameterization in the whole atmosphere community climate model: Motivation and results. *Journal of the Atmospheric Sciences*, *74*(1), 275–291. https://doi.org/10.1175/JAS-D-16-0104.1

Garcia, R. R., & Solomon, S. (1985). The effect of breaking gravity waves on the dynamics and chemical composition of the mesosphere and lower thermosphere. *Journal of Geophysical Research*, *90*(D2), 3850–3868. https://doi.org/10.1029/JD090iD02p03850

Gardner, C. S., Hostetler, C. A., & Franke, S. J. (1993). Gravity wave models for the horizontal wave number spectra of atmospheric velocity and density fluctuations. *Journal of Geophysical Research*, *98*(D1), 1035–1049. https://doi.org/10.1029/92JD02051

Gelaro, R., McCarty, W., Suárez, M. J., Todling, R., Molod, A., Takacs, L., et al. (2017). The modern-era retrospective analysis for research and applications, version 2 (MERRA-2). *Journal of Climate*, *30*(14), 5419–5454. https://doi.org/10.1175/JCLI-D-16-0758.1

Gibbons, S., Asming, V., Eliasson, L., Fedorov, A., Fyen, J., Kero, J., et al. (2015). The European Arctic: A laboratory for seismoacoustic studies. *Seismological Research Letters*, *86*(3), 917–928. https://doi.org/10.1785/0220140230

Gibbons, S., Kværna, T., & Näsholm, S. P. (2019). Characterization of the infrasonic wavefield from repeating seismo-acoustic events. In *Infrasound monitoring for atmospheric studies* (pp. 387–407). Springer. https://doi.org/10.1007/978-3-319-75140-5_10

Gibbons, S. J., Kværna, T., Tiira, T., & Kozlovskaya, E. (2020). A benchmark case study for seismic event relative location. *Geophysical Journal International*, *223*(2), 1313–1326. https://doi.org/10.1093/gji/ggaa362

Green, D. N., Waxler, R., Lalande, J.-M., Velea, D., & Talmadge, C. (2018). Regional infrasound generated by the Humming Roadrunner ground truth experiment. *Geophysical Journal International*, *214*(3), 1847–1864. https://doi.org/10.1093/gji/ggy232

Hamilton, M., & Blackstock, D. (2008). *Nonlinear acoustics*. Acoustical Society of America.

Hedlin, M. A., & Drob, D. P. (2014). Statistical characterization of atmospheric gravity waves by seismoacoustic observations. *Journal of Geophysical Research: Atmospheres*, *119*(9), 5345–5363. https://doi.org/10.1002/2013JD021304

Hines, C. O. (1991). The saturation of gravity waves in the middle atmosphere. Part II: Development of doppler-spread theory. *Journal of Atmospheric Sciences*, *48*(11), 1361–1379. https://doi.org/10.1175/1520-0469(1991)048⟨1361:TSOGWI⟩2.0.CO;2

IAP. (2023). Saura radar wind measurements [Dataset]. Leibniz Institute of Atmospheric Physics at the University of Rostock (IAP). https://doi.org/10.22000/918

Kinney, G. F., & Graham, K. J. (1985). *Explosive shocks in air* (2nd ed., p. 269). Springer.

Kulichkov, S. (2010). On the prospects for acoustic sounding of the fine structure of the middle atmosphere. In *Infrasound monitoring for atmospheric studies* (pp. 511–540). Springer. https://doi.org/10.1007/978-1-4020-9508-5_16

Kulichkov, S., Popov, O., Mishenin, A., Chunchuzov, I., Chkhetiani, O., & Tsybulskaya, N. (2017). Using the acoustic-pulse conservation law in estimating the energy of surface acoustic sources by remote sounding. *Izvestiya, Atmospheric and Oceanic Physics*, *53*(6), 603–612. https://doi.org/10.1134/S0001433817060068

Kumari, K., Wu, H., Long, A., Lu, X., & Oberheide, J. (2021). Mechanism studies of Madden-Julian oscillation coupling into the mesosphere/lower thermosphere tides using SABER, MERRA-2, and SD-WACCMX. *Journal of Geophysical Research: Atmospheres*, *126*(13), e2021JD034595. https://doi.org/10.1029/2021JD034595

Lalande, J.-M., & Waxler, R. (2016). The interaction between infrasonic waves and gravity wave perturbations: Application to observations using UTTR rocket motor fuel elimination events. *Journal of Geophysical Research: Atmospheres*, *121*(10), 5585–5600. https://doi.org/10.1002/2015JD024527

LANL. (2014). InfraGA/GeoAc [Software]. Los Alamos National Laboratory (LANL). Retrieved from https://github.com/LANL-Seismoacoustics/infraGA

Le Pichon, A., Assink, J. D., Heinrich, P., Blanc, E., Charlton-Perez, A., Lee, C. F., et al. (2015). Comparison of co-located independent ground-based middle atmospheric wind and temperature measurements with numerical weather prediction models. *Journal of Geophysical Research: Atmospheres*, *120*(16), 8318–8331. https://doi.org/10.1002/2015JD023273

Le Pichon, A., Blanc, E., & Drob, D. (2005). Probing high-altitude winds using infrasound. *Journal of Geophysical Research*, *110*(D20), D20104. https://doi.org/10.1029/2005JD006020

Le Pichon, A., Garcés, M., Blanc, E., Barthélémy, M., & Drob, D. P. (2002). Acoustic propagation and atmosphere characteristics derived from infrasonic waves generated by the Concorde. *The Journal of the Acoustical Society of America*, *111*(1), 629–641. https://doi.org/10.1121/1.1404434

Liu, H.-L., Bardeen, C. G., Foster, B. T., Lauritzen, P., Liu, J., Lu, G., et al. (2018). Development and validation of the Whole Atmosphere Community Climate Model with thermosphere and ionosphere extension (WACCM-X 2.0). *Journal of Advances in Modeling Earth Systems*, *10*(2), 381–402. https://doi.org/10.1002/2017MS001232

Liu, H.-L., McInerney, J., Santos, S., Lauritzen, P., Taylor, M., & Pedatella, N. (2014). Gravity waves simulated by high-resolution whole atmosphere community climate model. *Geophysical Research Letters*, *41*(24), 9106–9112. https://doi.org/10.1002/2014GL062468

Liu, J., Liu, H., Wang, W., Burns, A. G., Wu, Q., Gan, Q., et al. (2018). First results from the ionospheric extension of WACCM-X during the deep solar minimum year of 2008. *Journal of Geophysical Research: Space Physics*, *123*(2), 1534–1553. https://doi.org/10.1002/2017JA025010

Lonzaga, J. B. (2015). A theoretical relation between the celerity and trace velocity of infrasonic phases. *The Journal of the Acoustical Society of America*, *138*(3), EL242–EL247. https://doi.org/10.1121/1.4929628

Lonzaga, J. B., Waxler, R. M., Assink, J. D., & Talmadge, C. L. (2015). Modelling waveforms of infrasound arrivals from impulsive sources using weakly non-linear ray theory. *Geophysical Journal International*, *200*(3), 1347–1361. https://doi.org/10.1093/gji/ggu479

Marty, J. (2019). The IMS infrasound network: Current status and technological developments. In *Infrasound monitoring for atmospheric studies* (pp. 3–62). Springer. https://doi.org/10.1007/978-3-319-75140-5_1

McFarlane, N. (1987). The effect of orographically excited gravity wave drag on the general circulation of the lower stratosphere and troposphere. *Journal of Atmospheric Sciences*, *44*(14), 1775–1800. https://doi.org/10.1175/1520-0469(1987)044⟨1775:TEOOEG⟩2.0.CO;2

Melton, B. S., & Bailey, L. F. (1957). Multiple signal correlators. *Geophysics*, *22*(3), 565–588. https://doi.org/10.1190/1.1438390

Miller, A., Fritts, D., Chapman, D., Jones, G., Limon, M., Araujo, D., et al. (2015). Stratospheric imaging of polar mesospheric clouds: A new window on small-scale atmospheric dynamics. *Geophysical Research Letters*, *42*(14), 6058–6065. https://doi.org/10.1002/2015GL064758

Nippress, A., Green, D. N., Marcillo, O. E., & Arrowsmith, S. J. (2014). Generating regional infrasound celerity-range models using ground-truth information and the implications for event location. *Geophysical Journal International*, *197*(2), 1154–1165. https://doi.org/10.1093/gji/ggu049

Orsolini, Y. J., Limpasuvan, V., Pérot, K., Espy, P., Hibbins, R., Lossow, S., et al. (2017). Modelling the descent of nitric oxide during the elevated stratopause event of January 2013. *Journal of Atmospheric and Solar-Terrestrial Physics*, *155*, 50–61. https://doi.org/10.1016/j.jastp.2017.01.006

Pancheva, D., Mukhtarov, P., Hall, C., Meek, C., Tsutsumi, M., Pedatella, N., & Nozawa, S. (2020). Climatology of the main (24-h and 12-h) tides observed by meteor radars at svalbard and tromsø: Comparison with the models CMAM-DAS and WACCM-X. *Journal of Atmospheric and Solar-Terrestrial Physics*, *207*, 105339. https://doi.org/10.1016/j.jastp.2020.105339

Pilger, C., Ceranna, L., Ross, J. O., Vergoz, J., Le Pichon, A., Brachet, N., et al. (2018). The European infrasound bulletin. *Pure and Applied Geophysics*, *175*(10), 3619–3638. https://doi.org/10.1007/s00024-018-1900-3

Podglajen, A., Le Pichon, A., Garcia, R. F., Gérier, S., Millet, C., Bedka, K., et al. (2022). Stratospheric balloon observations of infrasound waves from the January 15 2022 Hunga eruption, Tonga. *Geophysical Research Letters*, *49*(19), e2022GL100833. https://doi.org/10.1029/2022GL100833

Popov, O., Mishenin, A., Kulichkov, S., Chunchuzov, I., Perepelkin, V., & Ceranna, L. (2022). The effect of the stratopause on the structure of the infrasound signal from the August 4, 2020, Beirut explosion. *The Journal of the Acoustical Society of America*, *152*(1), 99–106. https://doi.org/10.1121/10.0012191

Rapp, M., & Lübken, F.-J. (2004). Polar mesosphere summer echoes (PMSE): Review of observations and current understanding. *Atmospheric Chemistry and Physics*, *4*(11/12), 2601–2633. https://doi.org/10.5194/acp-4-2601-2004

Renkwitz, T., Tsutsumi, M., Laskar, F. I., Chau, J. L., & Latteck, R. (2018). On the role of anisotropic MF/HF scattering in mesospheric wind estimation. *Earth, Planets and Space*, *70*(1), 1–16. https://doi.org/10.1186/s40623-018-0927-0

Richter, J. H., Sassi, F., & Garcia, R. R. (2010). Toward a physically based gravity wave source parameterization in a general circulation model. *Journal of the Atmospheric Sciences*, *67*(1), 136–156. https://doi.org/10.1175/2009JAS3112.1

Sabatini, R., Snively, J. B., Bailly, C., Hickey, M. P., & Garrison, J. L. (2019). Numerical modeling of the propagation of infrasonic acoustic waves through the turbulent field generated by the breaking of mountain gravity waves. *Geophysical Research Letters*, *46*(10), 5526–5534. https://doi.org/10.1029/2019GL082456

Sassi, F., Liu, H.-L., Ma, J., & Garcia, R. R. (2013). The lower thermosphere during the northern hemisphere winter of 2009: A modeling study using high-altitude data assimilation products in WACCM-X. *Journal of Geophysical Research: Atmospheres*, *118*(16), 8954–8968. https://doi.org/10.1002/jgrd.50632

Schäfer, B., Baumgarten, G., & Fiedler, J. (2020). Small-scale structures in noctilucent clouds observed by lidar. *Journal of Atmospheric and Solar-Terrestrial Physics*, *208*, 105384. https://doi.org/10.1016/j.jastp.2020.105384

Selvaraj, D., Patra, A., Chandra, H., Sinha, H., & Das, U. (2014). Scattering cross section of mesospheric echoes and turbulence parameters from Gadanki radar observations. *Journal of Atmospheric and Solar-Terrestrial Physics*, *119*, 162–172. https://doi.org/10.1016/j.jastp.2014.08.004

Shaw, T. A., & Shepherd, T. G. (2008). Raising the roof. *Nature Geoscience*, *1*(1), 12–13. https://doi.org/10.1038/ngeo.2007.53

Singer, W., Latteck, R., & Holdsworth, D. (2008). A new narrow beam doppler radar at 3 MHz for studies of the high-latitude middle atmosphere. *Advances in Space Research*, *41*(9), 1488–1494. https://doi.org/10.1016/j.asr.2007.10.006

Siskind, D. E., Harvey, V. L., Sassi, F., McCormack, J. P., Randall, C. E., Hervig, M. E., & Bailey, S. M. (2021). Two- and three-dimensional structures of the descent of mesospheric trace constituents after the 2013 sudden stratospheric warming elevated stratopause event. *Atmospheric Chemistry and Physics*, *21*(18), 14059–14077. https://doi.org/10.5194/acp-21-14059-2021

Smets, P. S. M., & Evers, L. G. (2014). The life cycle of a sudden stratospheric warming from infrasonic ambient noise observations. *Journal of Geophysical Research: Atmospheres*, *119*(21), 12084–12099. https://doi.org/10.1002/2014JD021905

Smith, A. K. (2012). Global dynamics of the MLT. *Surveys in Geophysics*, *33*(6), 1177–1230. https://doi.org/10.1007/s10712-012-9196-9

Smith, S. A., Fritts, D. C., & Vanzandt, T. E. (1987). Evidence for a saturated spectrum of atmospheric gravity waves. *Journal of Atmospheric Sciences*, *44*(10), 1404–1410. https://doi.org/10.1175/1520-0469(1987)044⟨1404:EFASSO⟩2.0.CO;2

Stocker, T. F., Qin, D., Plattner, G.-K., Tignor, M. M., Allen, S. K., Boschung, J., et al. (2014). *Climate Change 2013: The physical science basis. Working group I contribution to the fifth assessment report of IPCC the intergovernmental panel on climate change* (pp. 741–866). Cambridge University Press. https://doi.org/10.1017/CBO9781107415324.020

Strelnikov, B., Eberhart, M., Friedrich, M., Hedin, J., Khaplanov, M., Baumgarten, G., et al. (2019). Simultaneous in situ measurements of small-scale structures in neutral, plasma, and atomic oxygen densities during the WADIS sounding rocket project. *Atmospheric Chemistry and Physics*, *19*(17), 11443–11460. https://doi.org/10.5194/acp-19-11443-2019

Tsuda, T. (2014). Characteristics of atmospheric gravity waves observed using the MU (Middle and Upper atmosphere) radar and GPS (Global Positioning System) radio occultation. *Proceedings of the Japan Academy, Series B*, *90*(1), 12–27. https://doi.org/10.2183/pjab.90.12

UCAR/NCAR. (2019). CCSM run SD-WACCM-X v2.1, atmosphere history data, 3-hourly instantaneous values (Version 7) [Dataset]. UCAR/NCAR - Climate and Global Dynamics Laboratory. https://doi.org/10.26024/5b58-nc53

Vadas, S. L., & Becker, E. (2018). Numerical modeling of the excitation, propagation, and dissipation of primary and secondary gravity waves during wintertime at McMurdo station in the Antarctic. *Journal of Geophysical Research: Atmospheres*, *123*(17), 9326–9369. https://doi.org/10.1029/2017JD027974

van Caspel, W. E., Espy, P. J., Ortland, D. A., & Hibbins, R. E. (2022). The mid-to high-latitude migrating semidiurnal tide: Results from a mechanistic tide model and SuperDARN observations. *Journal of Geophysical Research: Atmospheres*, *127*(1), e2021JD036007. https://doi.org/10.1029/2021JD036007

Vera Rodriguez, I., Näsholm, S. P., & Le Pichon, A. (2020). Atmospheric wind and temperature profiles inversion using infrasound: An ensemble model context. *The Journal of the Acoustical Society of America*, *148*(5), 2923–2934. https://doi.org/10.1121/10.0002482

Vorobeva, E., De Carlo, M., Le Pichon, A., Espy, P. J., & Näsholm, S. P. (2021). Benchmarking microbarom radiation and propagation model against infrasound recordings: A vespagram-based approach. *Annales Geophysicae*, *39*(3), 515–531. https://doi.org/10.5194/angeo-39-515-2021

Waugh, D. W., & Polvani, L. M. (2010). Stratospheric polar vortices. In *The stratosphere: Dynamics, transport, and chemistry* (pp. 43–57). American Geophysical Union (AGU). https://doi.org/10.1002/9781118666630.ch3

Waugh, D. W., Sobel, A. H., & Polvani, L. M. (2017). What is the polar vortex and how does it influence weather? *Bulletin of the American Meteorological Society*, *98*(1), 37–44. https://doi.org/10.1175/BAMS-D-15-00212.1

Waxler, R., & Assink, J. (2019). Propagation modeling through realistic atmosphere and benchmarking. In *Infrasound monitoring for atmospheric studies* (pp. 509–549). Springer. https://doi.org/10.1007/978-3-319-75140-5_15

Welch, P. (1967). The use of fast Fourier transform for the estimation of power spectra: A method based on time averaging over short, modified periodograms. *IEEE Transactions on Audio and Electroacoustics*, *15*(2), 70–73. https://doi.org/10.1109/TAU.1967.1161901

Wicker, W., Polichtchouk, I., & Domeisen, D. I. V. (2023). Increased vertical resolution in the stratosphere reveals role of gravity waves after sudden stratospheric warmings. *Weather and Climate Dynamics*, *4*(1), 81–93. https://doi.org/10.5194/wcd-4-81-2023

Zhang, J., Limpasuvan, V., Orsolini, Y. J., Espy, P. J., & Hibbins, R. E. (2021). Climatological westward-propagating semidiurnal tides and their composite response to sudden stratospheric warmings in SuperDARN and SD-WACCM-X. *Journal of Geophysical Research: Atmospheres*, *126*(3), e2020JD032895. https://doi.org/10.1029/2020JD032895